



# Rock characteristics and reservoir properties of Upper Carboniferous (Stephanian A–B) tight siliciclastic rocks from the Saar–Nahe basin (SW Germany)

Dennis Quandt<sup>1</sup> · Benjamin Busch<sup>1</sup> · Jonas Greve<sup>1,2,3</sup> · Christoph Hilgers<sup>1</sup>

Received: 13 October 2023 / Accepted: 26 January 2024  
© The Author(s) 2024

## Abstract

The environmental consequences of mine flooding in the Saar hard coal district, post-mining re-use concepts in the course of the energy transition, and the potential of coalbed methane production require an understanding of subsurface rock properties on the microscale. In this study, mineralogy, microtexture, microstructure, porosity, permeability, and geochemistry of an Upper Carboniferous (Stephanian A–B) drill core recovered in the Saar–Nahe basin are quantified. Based on these data, the diagenetic history and reservoir quality are analyzed regarding mine flooding and coalbed methane potential. The feldspar-poor and igneous rock fragment-free siliciclastic rock succession shows multiple fining upward sequences deposited in a fluvial environment during the pre-volcanic syn-rift phase of the Variscan intramontane Saar–Nahe basin. Intercalated small-scale coarsening upward sequences are related to the floodplain where near-surface soft-sediment deformation and paleosol formation took place. Porosity (<7%) of the tight siliciclastic rocks is mainly controlled by an interplay of authigenic microporous kaolinite, dissolution porosity, and quartz cement, whereas permeability (<0.05 mD) shows no systematic variation with petrography. During burial, quartz cements preserved porosity by stabilizing the granular framework against mechanical compaction, while phyllosilicates were ductilely deformed reducing reservoir quality. Relative phyllosilicates and quartz contents and mean grain size are reliably inferred from SiO<sub>2</sub>/Al<sub>2</sub>O<sub>3</sub> ratios (1.8–28.8), Ba (0.0108–0.0653 wt%), Rb (0.0024–0.0181 wt%), and Sr (0.0013–0.0086 wt%) concentrations measured with a portable x-ray fluorescence analyzer. Regarding coalbed methane production and mine flooding, sealing of cleats and heterogeneous subsurface rock properties due to dynamically changing depositional settings during the Late Carboniferous need to be considered.

**Keywords** Reservoir quality · Diagenesis · Upper Carboniferous · Tight sandstone reservoir · Saar hard coal mining · Variscan intramontane basin

## Introduction

The beneficial Late Carboniferous paleogeographic location of central Europe close to the equator with a humid tropical climate, the deposition of organic matter, and advantageous

burial paths resulted in the formation of numerous extractable hard coal seams in several central European foreland and intramontane basins (Opluštil and Cleal 2007; Cleal et al. 2009). One of these intramontane basins is the Saar–Nahe basin in SW Germany (Fig. 1a–b) where hard coal mining was abandoned in 2012 ahead of schedule after a series of mining-induced seismic events with a maximum magnitude of 4.0 in 2008 (Alber and Fritschen 2011).

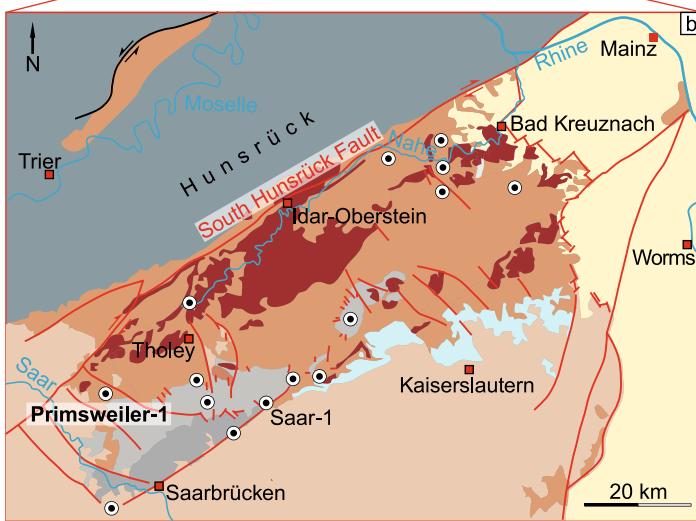
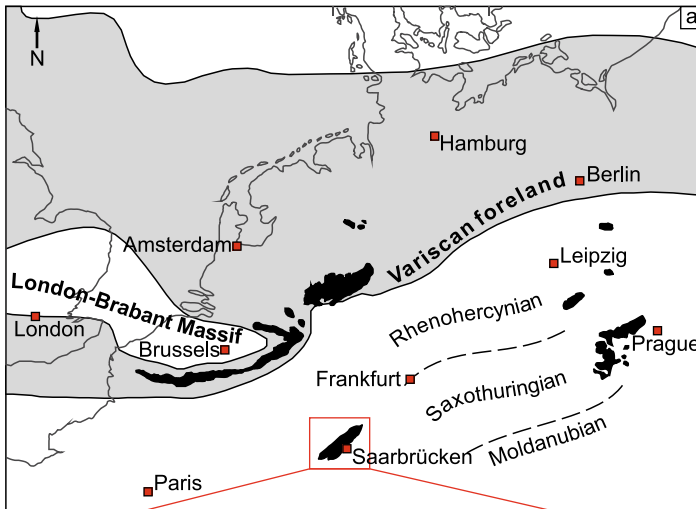
With the abandonment of the Saar hard coal district, costly mine water pumping became technically redundant and a controlled two-phase mine flooding process was initiated (Stemke and Wieber 2022). Mine flooding increases the pore fluid pressure of subsurface rocks affecting the local stress regime and thus may induce ground movements and micro-seismicity (e.g., Bischoff et al. 2010; Samsonov et al. 2013; Konicek et al. 2022; Rische et al. 2023; Declercq et al.

✉ Dennis Quandt  
dennis.quandt@kit.edu

<sup>1</sup> Institute of Applied Geosciences, Structural Geology and Tectonics, KIT – Karlsruhe Institute of Technology, Campus South, Adenauerring 20a, 76131 Karlsruhe, Germany

<sup>2</sup> Geological Survey North Rhine-Westphalia, De-Greif-Strasse 195, 47803 Krefeld, Germany

<sup>3</sup> Present Address: Stadtwerke Düsseldorf AG, Höherweg 100, 40233 Düsseldorf, Germany



Sys.	Stage	Group	Formation	Phase	
Lower Permian	Rotliegend	Late	Kreuznach Sponheim Wadern Donnersberg	Post-rift	
		Early	Tholey Lebach Kusel	Volcanic syn-rift	
	Late Carboniferous	Stephanian	D	Breitenbach	Pre-volcanic syn-rift
B			Heusweiler		
A			Dilsburg Göttelborn		
Westphalian		Saarbrücken Group	D	Heiligenwald Luidenthal	Proto-rift
			C	Geisheck Sulzbach	
			B	Rothell St. Ingbert	
			A	Neunkirchen	
Namurian			Spiesen		
Early	Visean			Pre-rift	
	Tournaisian				

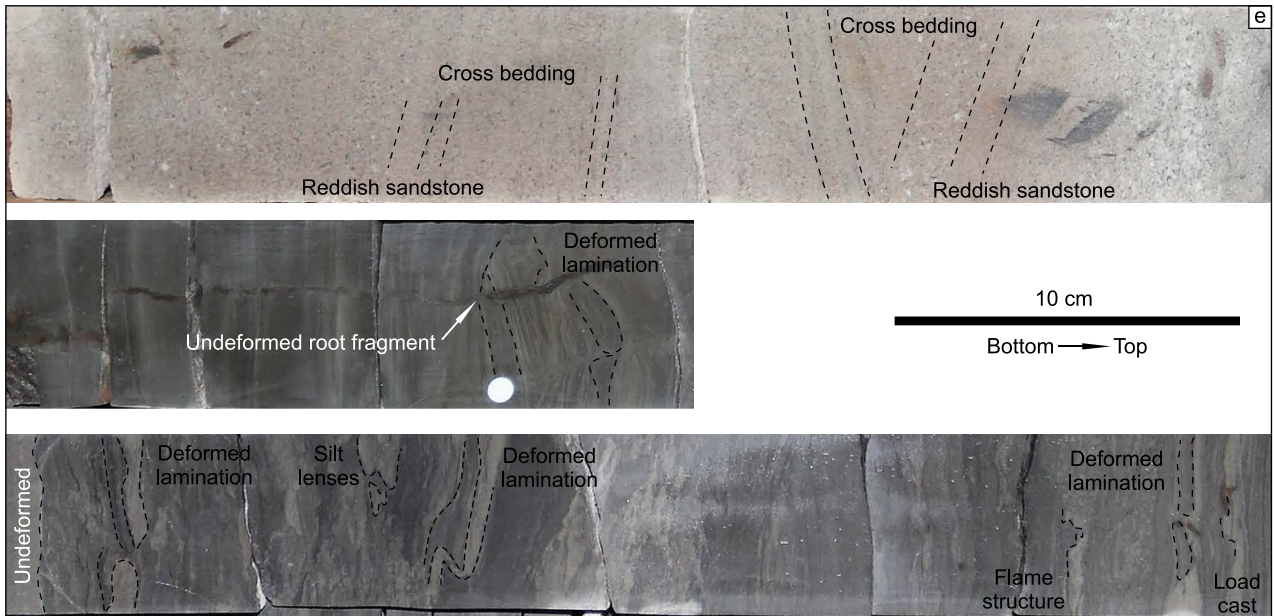
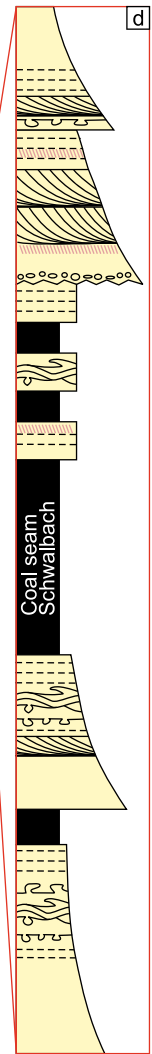


**Fig. 1** **a** Simplified paleogeographic map showing the Variscan tectonic units and coal basins in central Europe (modified after Brix et al. 1988 and Quandt et al. 2022a). **b** Simplified geological map of the Saar–Nahe basin (modified after Meschede 2018). **c** Lithostratigraphy of the Saar–Nahe basin (modified after Deutsche Stratigraphische Kommission 2016). **d** Simplified lithological column (not to scale) of the Stephanian A–B drill core logged in this study. **e** Photographs of parts of the drill core highlighting cross bedding in occasionally reddish sandstones and features indicative of soft-sediment deformation (e.g., load casts, flame structures, silt and sand lenses, deformed lamination)

2023; Quandt et al. 2023 and references therein). In regard of the energy transition and climate change, abandoned mining areas worldwide also open new possibilities for re-use comprising geothermal energy applications, carbon dioxide underground storage, unconventional gas production, and biomass production (e.g., Bungart and Hüttl 2001; Durucan et al. 2004; Piessens and Duser 2004; Busch et al. 2009; Wirth et al. 2012; Izart et al. 2016; Menéndez et al. 2019; Privalov et al. 2020; Everingham et al. 2022).

All these industrial applications have in common that they require an understanding of the reservoir quality, which is addressed in this study. In general, reservoir quality is a function of porosity and permeability and depends on depositional and diagenetic processes (e.g., Stonecipher et al. 1984; Burley et al. 1985; Worden et al. 2018). Among others, depositional and diagenetic processes comprising erosion, transport, deposition, burial, alteration, cementation, mechanical compaction, and uplift under specific physicochemical conditions (e.g., pressure, temperature, fluid composition, time) control grain size, grain sorting, detrital and authigenic mineralogy, rock texture, and structure (e.g., Bloch 1991; Ajdukiewicz and Lander 2010; Morad et al. 2010, 2012; Taylor et al. 2010; Bjørlykke and Jahren 2012; Worden et al. 2018). Thus, the quantitative analysis of these petrographic properties coupled with laboratory measured porosity and permeability values enables the determination of the crucial factors on reservoir quality (e.g., Becker et al. 2017, 2019; Wüstefeld et al. 2017a; Busch et al. 2019, 2020, 2022a; b; Quandt et al. 2022a, b).

Previously published geoscientific studies on the Saar–Nahe basin focused on its tectonic evolution using DEKORP seismic reflection profiles (e.g., Korsch and Schäfer 1991; Henk 1993a, b), the basin fill history based on analyses of sedimentary and igneous rock successions (e.g., Schäfer 1989; Stollhofen and Stanistreet 1994; Stollhofen 1998), and the burial history inferred from vitrinite reflectance and apatite fission track data (Littke et al. 2000; Izart et al. 2016). These studies were complemented by industrial hard coal mining activities including reconnaissance drilling campaigns and hard coal seam mappings (Schäfer 1989; Juch et al. 1994). Taken together, these comprehensive data make the Saar–Nahe basin into a well-studied area in terms

of its geological evolution (Schäfer 1989). However, published studies on its diagenetic history and reservoir quality of such tight gas analogs are scarce and limited to a very few publications (Durucan et al. 2004; Aretz et al. 2016).

Here, we present a study on petrographical, petrophysical, and geochemical properties of a section of an Upper Carboniferous drill core from the Saar hard coal district. Depositional and diagenetic processes of the siliciclastic rocks are quantified by optical microscopy and point counting, and correlated with laboratory measured porosity and permeability values as well as portable X-ray fluorescence (pXRF) whole-rock geochemical compositions. Based on these data, the diagenetic history is interpreted, the reservoir quality is evaluated, and the reservoir quality-controlling factors are assessed. Furthermore, microstructural analyses of (partially) mineralized cleats in coal are used to assess their influence on porosity and permeability. In addition, pXRF-derived geochemical compositions are correlated with petrographic features to evaluate the reliability of this technique and to test if textural and mineralogical properties can be inferred from pXRF geochemistry. This may enable the prediction of reservoir quality (e.g., Scherer 1987) of cutting material in case drill core material is not available. Our findings are placed within the regional geological framework and discussed in the context of mine flooding and coalbed methane potential. Since published literature on diagenesis and reservoir data on the Saar hard coal district is scarce (Durucan et al. 2004; Aretz et al. 2016), this study fills a data gap.

## Geological setting

The drill core studied here was recovered in the Saar–Nahe basin (Fig. 1b), which extends over 100 km from Bad Kreuznach, situated SW of Frankfurt on the Main, to Saarbrücken, Germany. It constitutes an asymmetric half-graben with Variscan anticlines and synclines whose folding axes are oriented parallel to the strike of the basin (e.g., Stollhofen and Stanistreet 1994; Korsch and Schäfer 1995; Stollhofen 1998). The formation of the Variscan intramontane Saar–Nahe molasse basin was controlled by the South Hunsrück Fault that defines the northern boundary of the basin (Fig. 1a) (Korsch and Schäfer 1995). Basin formation was related to dextral strike-slip faulting creating a transtensional basin and, contrastingly, Variscan thrust fault reactivation forming a listric normal fault (e.g., Meissner et al. 1980, 1984; Anderle 1987; Korsch and Schäfer 1991; Henk 1993a, b; Schäfer 2011).

Drill cores recovered by the hydrocarbon industry (Fig. 1b) provide insights into the entire approximately 8 km thick Early Permian to Late Carboniferous molasse basin fill and its underlying basement (Schäfer 1989, 2011). The

basement and the different sedimentary successions filling the basin were subdivided into pre-rift, proto-rift, pre-volcanic and volcanic syn-rift, and post-rift phases (Fig. 1c; Henk 1993a; Stollhofen and Stanistreet 1994). The onset of basin formation was attributed to the latest Namurian (Spiesen Fm.; Korsch and Schäfer 1995). The Namurian basin fill consists of coarse conglomerates and an upward fining sandstone succession probably associated with an alluvial fan or fluvial depositional system (Schäfer and Korsch 1998). These sedimentary rocks correspond to the proto-rift phase that continues into the Westphalian A–D (Saarbrücken Gr.; Schäfer and Korsch 1998; Stollhofen 1998).

The Westphalian basin fill is characterized by argillaceous sandstones that were deposited in fluvial (Westphalian A–C) and deltaic (Westphalian C–D) environments in a tropical climate (Schäfer et al. 1990; Schäfer and Korsch 1998; Schäfer 2011). Coals seams lack in Westphalian A strata, but become abundant in Westphalian B–D strata. Sediments were sourced from the Rhenohercynian (i.e., Rhenish Massif) where quartzitic sandstones and slates were eroded and subsequently transported by braided and meandering rivers as indicated by well-rounded clasts (Schäfer 2011). Westphalian strata document the proto-rift phase of the Saar–Nahe basin (Stollhofen 1998; Schäfer 2011).

From the Westphalian to the Stephanian (Ottweiler Gr.) and Early Rotliegend (Glan Gr.), the Saar–Nahe basin underwent progressive geological and climatic changes. The sedimentary source area changed from the northern Rhenohercynian (i.e., Rhenish Massif) to the southern Moldanubian (i.e., Black Forest, Vosges, Massif Central). Coincidentally, deltaic depositional environments associated with lakes gained in importance relative to meandering and braided fluvial settings, which dominated in the previous Westphalian A–C (Schäfer 2011). The Stephanian corresponds to the pre-volcanic syn-rift phase and is mainly characterized by upward coarsening successions (Stollhofen 1998), which consist of reworked Westphalian siliciclastics, shales, rounded to well-rounded arkosic sandstones and arkoses with high contents of detrital feldspar, as well as minor conglomerates, limestones, and coal seams (Schäfer 1986; Stollhofen 1998; Schäfer 2011 and references therein). Thus, the Stephanian lithostratigraphy shows a high variation in rock color and grain size with conglomerates becoming more abundant in the Stephanian–Rotliegend boundary (Schäfer 1989).

The subsequent Early Rotliegend marks the onset of the volcanic syn-rift phase (Stollhofen 1998). Igneous rocks are intercalated with limestones and siliciclastic rocks. Furthermore, the tropical climate of the Westphalian transitions into a sub-tropical climate during the Stephanian and Early Rotliegend (Schäfer and Sneh 1983; Roscher and Schneider 2006; Schäfer 2011). Consequently, coal seams become

progressively sparser from the Stephanian to Early Rotliegend (Schäfer 2011). The termination of major tectonic extension and igneous activity in the Late Rotliegend marks the onset of the post-rift phase (Stollhofen 1998). In the Late Rotliegend (Nahe Gr.), a hot arid climate prevails and results in the deposition of fining upward red beds. Deposition took place in alternating environments comprising alluvial, fluvial, lacustrine (playa lakes), and eolian settings without coal (Schäfer 2011).

Burial depth culminated in Late Carboniferous to Early Permian (Hertle and Littke 2000; Littke et al. 2000). Deposition probably persisted until the Cretaceous (Henk 1993b), but was interrupted by a temporary uplift phase in the Late Permian accompanied by an erosional event that removed up to 2 km of the sedimentary succession (Henk 1993a; Littke et al. 2000; Izart et al. 2016). In the Jurassic to Early Cretaceous, the base of the Stephanian A reached its maximum burial temperature of 120–150 °C during a reheating phase, possibly caused by the opening of the Atlantic Ocean (Littke et al. 2000; Izart et al. 2016). Subsequent uplift beginning in Early Cretaceous times exposed the Saar–Nahe basin fill again to erosion. This was followed by a hiatus that lasted until the Oligocene (Henk 1993b; Littke et al. 2000).

## Methods

### Material, core logging, and sampling

In this study, a cored interval of 29 m from the drill core Primsweiler-1 (1753.15–1782.15 m NN, WGS84 N 49.397089 E 6.848970, depth: 204.62 m NN) is investigated. According to the unpublished well report by the Saar hard coal mine (Bergwerk Saar) from 1991, the drill core covers the top of the Stephanian A (upper Dilsburg Fm.) and the base of the Stephanian B (lower Heusweiler Fm.; Fig. 1c–d). The Stephanian A–B boundary is marked by the coal seam Schwalbach (Bhardwaj 1955; Uhl and Jasper 2021). This coal seam is also documented in the unpublished well report by the Saar hard coal mine. Core logging involved the macroscopic determination of grain size and grading, structures such as fractures and bedding type, secondary mineralization, and fossil and trace fossil contents at the Geological Survey North Rhine–Westphalia core store in Krefeld, Germany. These observations were considered for the construction of the lithological column using the software EasyCore (The EasyCopy Company).

Representative sections of the drill core were sampled parallel to bedding using a drill press. The cylindrical one-inch diameter plugs were then cut to length to ensure cylindricality. Remaining trim ends were used for preparation of ca. 30 µm thick thin sections. Thin sections were impregnated with blue-dyed epoxy resin and stained by a combination of Alizarin

red S and potassium ferricyanate in dilute HCl. This enables the identification of blue pore space and the differentiation between carbonate minerals.

## Petrography

Mean grain sizes of each sample were measured using image analysis of thin section microphotographs. For this purpose, a grid adjusted to the maximum grain size per sample observed during thin section microscopy was applied. Subsequently, the long axes of 100 grains per sample were measured. Based on the grain sizes determined, sorting and skewness were calculated according to Folk and Ward (1957).

Modal mineralogical and textural analyses were conducted using a semi-automatic point counting stage attached to a transmitted light microscope. Step length was adjusted to the maximum grain size observed in each sample. Per sample 300 points were counted yielding statistically reliable results (Ingersoll et al. 1984). Each point count was attributed to a category shown in Table A (Online Resources). These categories comprise detrital and authigenic minerals as well as textural components such as porosity subdivided into intergranular, dissolution, and fracture porosity. Fractures are distinguished from cleats. Cleats studied here refer to opening-mode fractures (Laubach et al. 1998) in coal fragments and millimeter-thick coal seams.

Total point counts were normalized to 300 to obtain percentages. In addition, points counted as detrital quartz, feldspar, and rock fragment were normalized to their total sum to plot the normalized values in the ternary QFR (quartz, feldspar, rock fragment) diagram after Folk (1980). These values are referred to as normative quartz, feldspar, and rock fragments.

Based on point counting results, the intergranular volume (IGV), compactional porosity loss (COPL), cementational porosity loss (CEPL), and compaction index (ICOMPACT) were calculated. The IGV represents the sum of intergranular pore space  $P_{\text{intergranular}}$ , intergranular cements  $C_{\text{intergranular}}$ , and depositional matrix  $M_{\text{depositional}}$  (Eq. 1) Paxton et al. 2002). COPL and CEPL are a function of initial porosity  $P_i$ , total optical porosity  $P_o$ , total pore-filling cement  $C$ , and minus cement porosity  $P_{\text{mc}}$ . The latter represents the sum of  $P_o$  and  $C$  (Eqs. 2 and 3, Lundegard 1992). An initial porosity of 45% typical for fluvial sediments were consistently used for calculations (Lundegard 1992). ICOMPACT represents the ratio of COPL to the sum of COPL and CEPL (Eq. 4, Lundegard 1992).

$$\text{IGV} = P_{\text{intergranular}} + C_{\text{intergranular}} + M_{\text{depositional}} \quad (1)$$

$$\text{COPL} = P_i - \frac{((100 - P_i) \times P_{\text{mc}})}{(100 - P_{\text{mc}})} \quad \text{with } P_{\text{mc}} = P_o + C \quad (2)$$

$$\text{CEPL} = (P_i - \text{COPL}) \times \frac{C}{P_{\text{mc}}} \quad (3)$$

$$\text{ICOMPACT} = \frac{\text{COPL}}{\text{COPL} + \text{CEPL}} \quad (4)$$

## Petrophysics

Prior to any petrophysical measurement, rock plugs were dried in a vacuum oven for 2 days at 40 °C. Klinkenberg-corrected permeability of cylindrical rock plugs was measured using an air permeameter (Westphal Mechanik) at steady state with a confining pressure of 1.2 MPa at the Institute of Structural Geology and Tectonics, Institute of Applied Geosciences, Karlsruhe Institute of Technology. Dry and oil-free lab air (80% N<sub>2</sub>, 20% O<sub>2</sub>) served as the permeant (Klinkenberg 1941, Rieckmann 1970).

Density of rock plugs with known dimensions (length and diameter) was measured using a semi-automated micromeritics Accupyc II 1340 helium pycnometer at the Institute of Structural Geology and Tectonics, Institute of Applied Geosciences, Karlsruhe Institute of Technology, Germany. Based on rock plug volume obtained by this measurement and rock plug dimensions measured with a caliper, sample porosity was calculated.

## Whole-rock pXRF geochemistry

Elemental concentrations from Mg to U were determined using a Bruker S1Titan800 pXRF analyzer at the Institute of Structural Geology and Tectonics, Institute of Applied Geosciences, Karlsruhe Institute of Technology, Germany. The analyzer was operated with an electric power of 4 W, a maximum electric current of 200 μA, and a maximum voltage of 50 kV. It is equipped with a Rh-target X-ray tube, a Graphene window silicon drift detector, and an Ultralene window. Elemental concentrations were determined in the GeoExploration software mode. Sample measurements were performed on the same plugs that were also used for petrophysical methods and thin section production. The plugs have smooth circular surfaces larger than the instrument window and are thus well-suitable for pXRF analyses regarding data reliability and radiation protection. Before and after measuring the sample series, the in-house standard CS-M2 provided by Bruker was measured ten times to ensure precision and accuracy of the instrument. Each sample and standard measurement lasted three times 20 s. Mean values for Al<sub>2</sub>O<sub>3</sub>, K<sub>2</sub>O, Ca, Mn, Fe, Cu, and Pb are within the respective minimum and maximum acceptance limits reported by Bruker. Lack of major oxide or element data for single or multiple samples resulted in the omission of all analyses of this specific element. Consequently, only

concentrations of MgO, Al<sub>2</sub>O<sub>3</sub>, SiO<sub>2</sub>, K<sub>2</sub>O, Ca, Fe, Ti, Mn, Cr, Ni, Ni, Cu, Zn, Rb, Sr, Y, Zr, Ba were considered in this study.

## Results

### Lithology

The logged core section is characterized by a 29 m thick sequence of alternating siliciclastic rocks with mean grain sizes varying from silt to very coarse sand (Fig. 1d–e and Fig. A, Online Resources). Three approximately 10 m thick fining upward sequences are distinguished. Their bases are composed of fine to very coarse sandstones overlain by finer sandstones and siltstones with 0.1–1.7 m thick coal seams on top. Locally, the large-scale fining upward sequences are interrupted by cm-thick coarser sandstones defining small-scale coarsening upward sequences. The contacts between the sequences are sharp.

The lowermost sandstones of the section are massive and structureless and show greenish gray to gray colors. Toward the top, faintly wavy or horizontally planar laminated, low-angle planar laminated (5–10° dip), and planar cross-bedded (up to 30° dip) sandstones become increasingly prominent. Similarly, intercalated reddish sandstones become more abundant toward the top (Fig. 1e). The bottom of a section of cross-bedded sandstones is marked by an erosional contact (– 1762.67 m). Siltstones are massive or wavy to horizontally planar laminated. These laminations may be disturbed resulting in convolute lamination that is also observed among some sandstones. Convolute lamination is spatially accompanied by load casts and flame structures with related silt and sand lenses within a finer grained matrix forming pseudo-nodules. Convolute lamination extends over a few centimeters in thickness and transitions downwards and upwards into undisturbed laminated or structureless siliciclastic rocks. In addition, convolute bedding is crosscut by an approximately 50 cm long, undeformed root fragment (Fig. 1e). Locally, siltstones exhibit a patchy, irregular reddening.

Fractures are commonly mineralized forming veins and are bedding parallel or steeper than 45°. Non-mineralized fractures are horizontally to sub-horizontally oriented. Slickenlines and microfractures have been observed but are scarce.

### Petrography

Mean grain sizes range from 0.006 to 0.251 mm corresponding to silt, very fine sand, fine sand, and medium sand fractions. Sorting coefficients vary between 0.6 and 1.5 comprising moderately well, moderately, and poorly sorted samples.

Skewness values range between – 0.2 and 0.4 corresponding to coarse, nearly symmetrical, fine skewed, and strongly fine skewed samples. Fine and very fine silt samples are characterized by low sorting coefficients < 0.7 and negative skewness. Coarse silt and coarser samples show the whole range of sorting coefficients and consistently positive skewness (Fig. 2). Grain contacts range from long to concavo-convex to sutured contacts.

Most samples ( $n = 23$ ) are composed of > 80% detrital quartz and rock fragments, while K-feldspar and plagioclase are almost absent (one point count each) (Fig. 3a–h). Consequently, the samples are classified as litharenites and sublitharenites with coarser samples being richer in quartz (up to 77.3% normative quartz) and finer samples being richer in rock fragments (up to 97.3% normative rock fragments) (Fig. 4a).

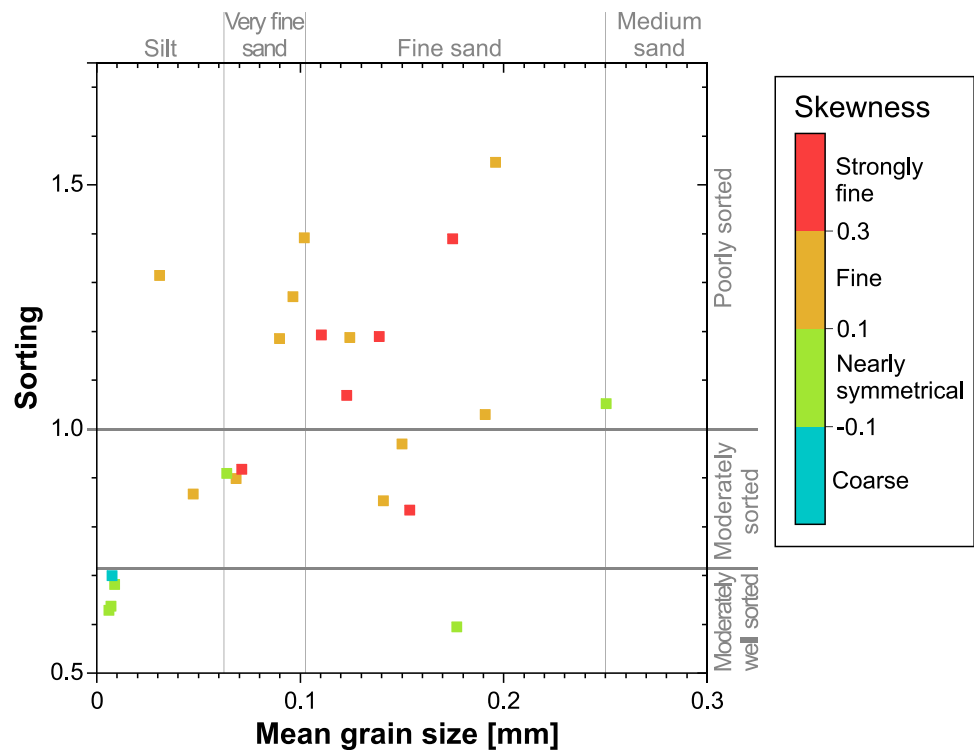
Rock fragments are dominantly metamorphic comprising phyllites (0–13.0%) and quartzite (0–1.3%) and subordinately siliciclastic like shale (0–8.7%), siltstone (0–2.7% in average per sample), sandstone (0–2.0% in average per sample), and chert (0–0.7% in average per sample) (Fig. 4b). Igneous rock fragments are absent. Muscovite (0–1.3% per sample), chlorite (0–0.7% per sample), titanite (0–0.7% per sample), and zircon (0–0.3% per sample) are accessory detrital minerals.

The remaining < 20% components encompass paleosol (0.0–15.0% omitting one sample with 55.3%), authigenic cement phases (0–6.3% per sample), porosity (0–5.0% per sample), coal fragments (0.0–4.7% per sample), and detrital accessories (0–2.0% per sample) in order of decreasing abundance. Coal fragments are oriented parallel to bedding and are commonly associated with (partially) mineralized and non-mineralized fractures (i.e., cleats). Cleats are oriented parallel (horizontal, non-mineralized) and normal (vertical) to the bedding-parallel coal fragments. Vertical cleats may be filled with quartz (Fig. 3h) or Fe-rich carbonate cements.

Paleosols are composed of siderite or calcite. Siderite paleosol occurs as spherulitic nodules with radial extinction (Fig. 3e) or as granular, partly microcrystalline, aggregates with high relief finely dispersed within the paleosol pseudomatrix. Spherulitic siderite is rare and restricted to silt-size samples and spatially associated with coal fragments, whereas the more common granular and microcrystalline aggregates occur in rocks of all grain sizes. Calcite paleosol is less common than siderite paleosol and composed of microcrystalline aggregates surrounded by isopachous fibrous to elongate blocky calcite and radial fibrous nodules (Fig. 3f).

Among the authigenic cements (Fig. 3b–c), syntaxial quartz is the most abundant cement phase (0–5.0% per sample) followed by calcite including Fe-calcite (0–4.0% per sample). Quartz cements show optical continuity with

**Fig. 2** Sorting coefficients plotted against mean grain size with skewness indicated by a color code. Thresholds are taken from Folk (1980)



their detrital grains. Detrital quartz grains are typically rich in fluid inclusions, whereas their overgrowth are fluid inclusion-poor enabling distinction between them. Syntaxial quartz cements often show euhedral crystal facets adjacent to kaolinite booklets (Fig. 3d). Where syntaxial quartz cement is in contact with calcite or Fe-calcite, quartz overgrowths usually show better developed crystal facets than calcite cements. Calcites may have an Fe-rich core and thin Fe-poor rim. Between the different cements, interlocking contacts are observed.

Authigenic kaolinite (0–3.3% per sample) occurs as a replacement with the original grain shapes preserved. Kaolinite developed characteristic booklet textures with microscopic intragranular porosity. Kaolinite may be partially replaced by chlorite (0–0.3%) with a carbonate phase and quartz in close spatial association (Fig. 3d). Chlorite also replaces rock fragments and feldspar (0–0.3%) and is typically characterized by a green color and anomalous dark blue interference colors.

Total optical porosity mainly represents intragranular dissolution porosity (0–5.0% per sample) related to the dissolution of rock fragments (0–5.0% per sample) and non-mineralized fractures (0–0.3% per sample). These fractures are typically oriented along coal fragments. Intergranular porosity is almost absent (0–0.3% per sample, two point counts in total).

## Compaction

Shale, slate, phyllite, and schist rock fragments, paleosol, coal fragments, detrital muscovite, and chlorite show a ductile deformation behavior along rigid detrital components such as quartz and their syntaxial overgrowths. Taken together, the sum of all ductile components per sample ranges from 15.7 to 99.0%. IGV values range from 0.0 to 6.3% resulting in a mean IGV of 2.3%. Samples consistently have COPL values > 39% up to 45%. CEPL values are consistently < 4% (Fig. 5).

## Petrophysics

Sample densities are between 2.6 and 3.3 g/cm<sup>3</sup> with most values ( $n = 22$ )  $\leq 2.8$  g/cm<sup>3</sup> resulting in a mean density of 2.7 g/cm<sup>3</sup>. Porosity varies between 0.6 and 7.0% (Fig. 6). The mean porosity of the sample set is 3.4% (Fig. 6). Permeability ranges from values below detection limit (i.e., 0.0001 mD,  $n = 2$ ) to 0.0481 mD. Mean permeability of the sample set is 0.0102 mD.

## Geochemistry

The major element oxides SiO<sub>2</sub> and Al<sub>2</sub>O<sub>3</sub> are the main geochemical components making up > 75% of the geochemical

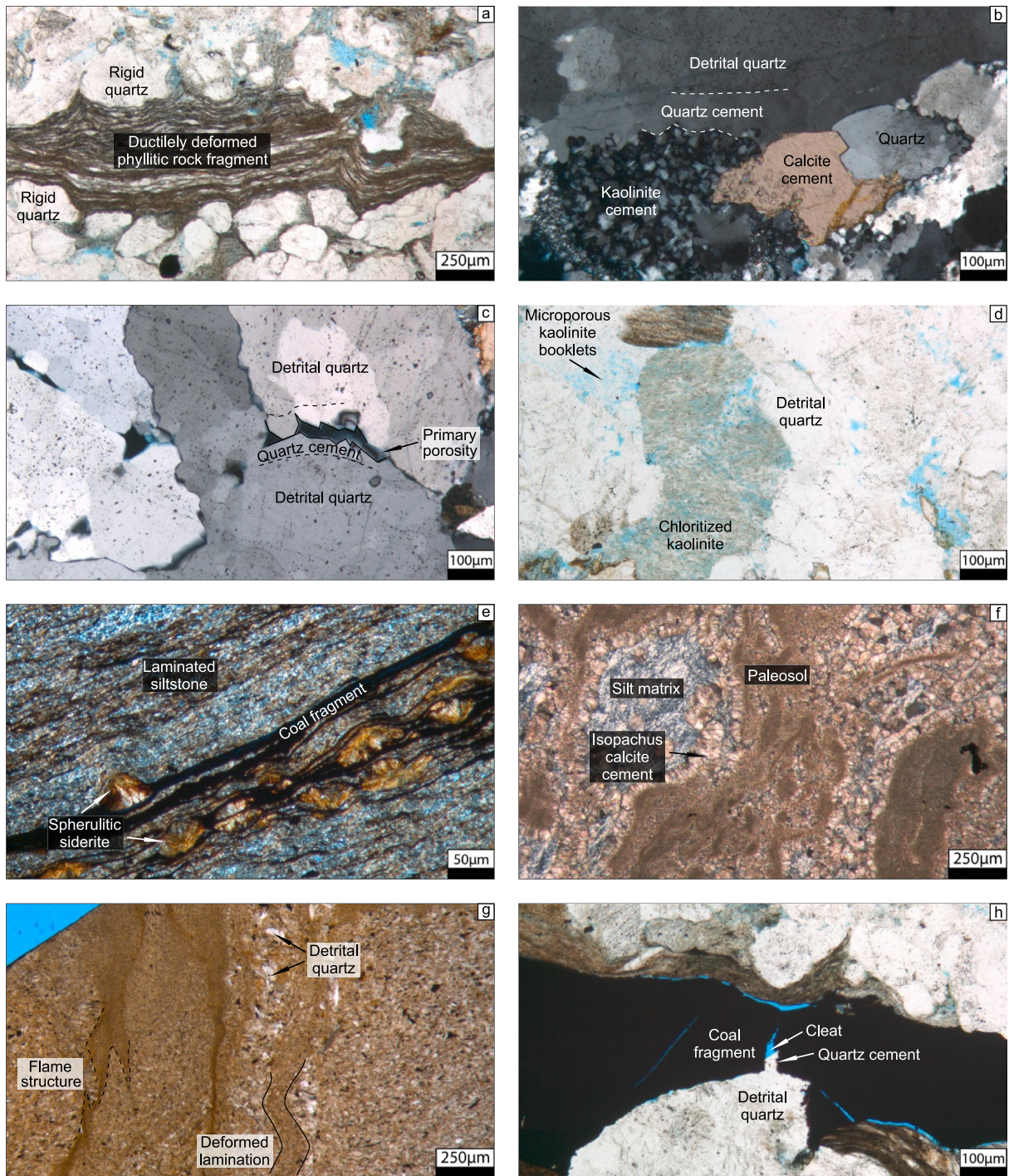


**Fig. 3** Thin section microphotographs. **a** Ductilely deformed phyllitic rock fragment between rigid quartz grains with syntaxial overgrowths (PW04, parallel polarized light, ppl). **b** Interlocking grain contacts between authigenic quartz, calcite, and kaolinite (PW08, cross polarized light, xpl). **c** Syntaxial quartz cements in contact with each other preserving (dark blue) primary porosity (PW08, ppl). **d** Chloritized kaolinite and secondary porosity due to dissolution of rock fragments (PW08, ppl). Original microporosity of kaolinite booklets is preserved after chloritization. **e** Euhedrally developed sideritic spherulites spatially associated with thin coal seams in a siltstone sample

(PW12, xpl). In contrast to coal fragments, siderite spherulites do not show evidence of plastic deformation. **f** Calcite paleosol consisting of microcrystalline aggregates surrounded by isopachous fibrous to elongate blocky calcite and radial fibrous nodules (PW20, xpl). **g** Deformed horizontal lamination and flame structures give evidence of soft-sediment deformation in a siltstone sample (PW21, ppl). **h** Vertical cleat in coal fragment partially filled with syntaxial quartz cement (PW11, ppl). Horizontal cleats are commonly non-mineralized

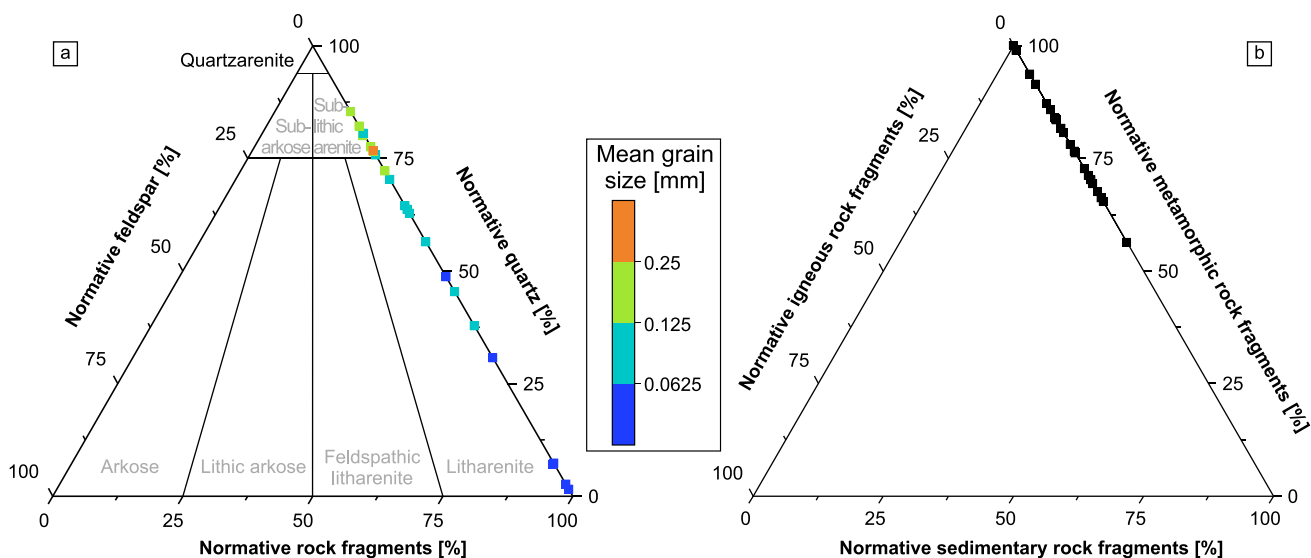


**Fig. 4** **a** Ternary classification of sandstones and siltstones based on normalized quartz, feldspar, and rock fragment contents according to Folk (1980). Colors indicate mean grain size. **b** Ternary diagram showing type of rock fragments

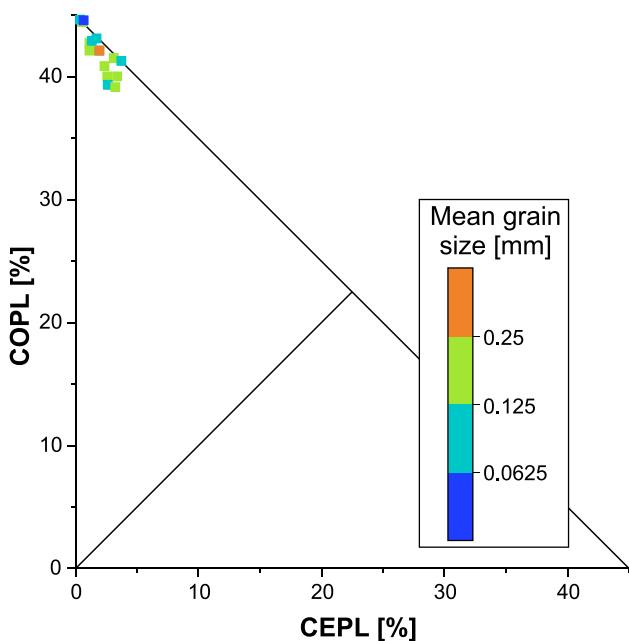


**Fig. 5** Compaction porosity loss (COPL) plotted against cementation porosity loss (CEPL). Color code indicates mean grain size

composition of most samples ( $n = 23$ ). The proportions of  $\text{SiO}_2$  (16.1–97.0 wt%) and  $\text{Al}_2\text{O}_3$  (3.4–24.8 wt%) per sample vary significantly resulting in  $\text{SiO}_2/\text{Al}_2\text{O}_3$  ratios between 1.8 and 28.8 (Table A, Online Resources). Further major geochemical components are Fe (0.7–37.0 wt% per sample),  $\text{K}_2\text{O}$  (0.6–4.1 wt%), MgO (0.4–3.6 wt%), Ca (0.1–3.5 wt%), Ti (0.1–1.5 wt%), and Mn (0.0–1.5 wt%). Ba (0.0108–0.0653 wt%), Rb (0.0024–0.0181 wt%), Sr (0.0013–0.0086 wt%),

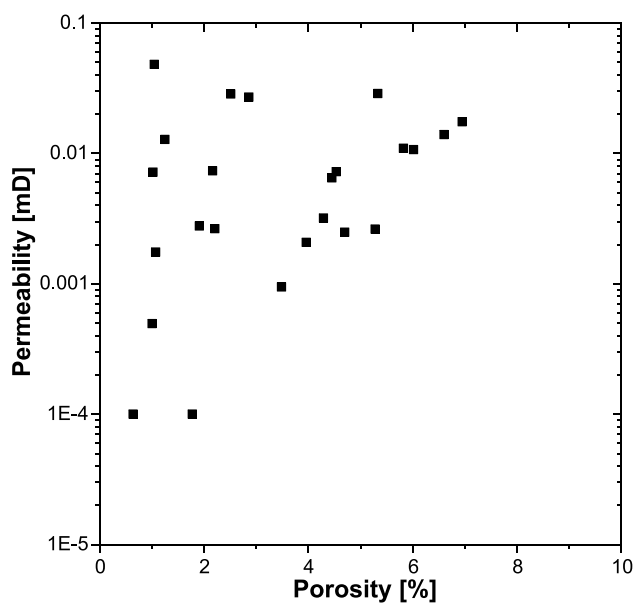


**Fig. 6** Porosity–Permeability cross plot. Samples with permeability values at 0.0001 mD are below detection limit

Cr (0.0044–0.0202 wt%), Ni (0.0013–0.0365 wt%), Cu (0.0006–0.0051 wt%), Zn (0.0015–0.0228 wt%), Y (0.0006–0.0039 wt%), and Zr (0.0008–0.0711 wt%) occur as trace elements (Table A, Online Resources).

**Correlations between petrophysics and petrography**

The cross plot of porosity against permeability reveals two features: a point cloud with a weak positive correlation ( $R^2 = 0.05$ ) for samples with porosity < 3% and a positive

trend ( $R^2=0.4$ ) for samples with porosity  $> 3\%$  (Fig. 6). Correlations are observed between petrographic features and porosity values. In contrast, permeability values do not show any systematic correlation with petrographic features. In order of decreasing significance, correlations with porosity are observed for (1) kaolinite content (Fig. 7a), (2) quartz cement content (Fig. 7b), (3) secondary porosity (Fig. 7c), (4) IGV (Fig. 7d), (5) COPL (Fig. 7e), (6) CEPL (Fig. 7f), (7) ductile component content (Fig. 7g), (8) mean grain size (Fig. 7h), and (9) coal fragment content (Fig. 7i). Among

these factors, kaolinite, quartz cements, secondary porosity, IGV, CEPL, and grain size are positively correlated with porosity, whereas COPL, ductile components, and coal fragments show negative correlations.

### Correlations between geochemistry and petrography

$\text{SiO}_2$  concentrations show good ( $R^2 \geq 0.6$ ) to very good ( $R^2 \geq 0.8$ ) negative correlations with  $\text{Al}_2\text{O}_3$  ( $R^2 = 0.81$ ),

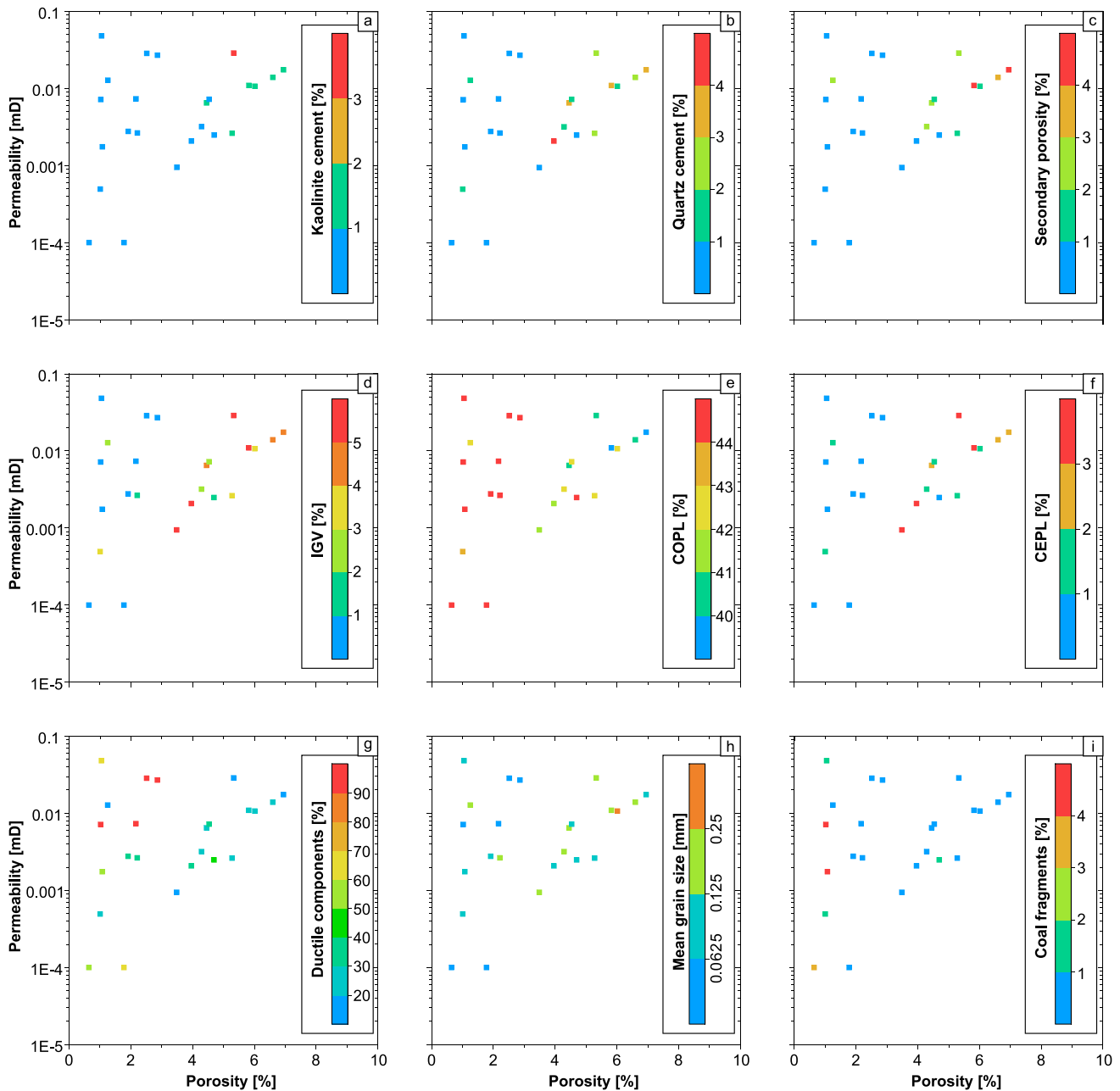


**Fig. 7** Porosity and permeability values plotted against **a** authigenic kaolinite, **b** quartz cement, **c** secondary porosity, **d** IGV, **e** COPL, **f** CEPL, **g** ductile components, **h** mean grain size, and **i** coal fragments

$K_2O$  ( $R^2=0.81$ ),  $MgO$  ( $R^2=0.83$ ),  $Ba$  ( $R^2=0.81$ ),  $Rb$  ( $R^2=0.80$ ), and  $Sr$  ( $R^2=0.68$ ) when sample PW20 with a relative high Fe content (37 wt%) is excluded (Fig. 8). Similarly, Fe ( $R^2=0.75$ ) and Ti ( $R^2=0.66$ ) reveal good-negative correlations when samples with high Fe concentrations  $\geq 19\%$  (PW16, PW20) and samples with high (1.5 wt%) and low Ti (0.11 wt%) concentrations (PW09, PW20) are excluded, respectively (Fig. 8). Further very good positive correlations exist for  $K_2O$  with  $Ba$  ( $R^2=0.97$ ) and  $Rb$  ( $R^2=0.99$ ) (Fig. 9). Moreover, good ( $R^2 \geq 0.6$ ) to very good correlations ( $R^2 \geq 0.8$ ) are observed between point counting results and major element oxide and trace element concentrations (Figs. 10, 11). Both,  $SiO_2$  and  $Al_2O_3$ , show good to very good opposing correlations with total quartz content ( $R^2=0.85, 0.96$ ), detrital quartz content ( $R^2=0.84, 0.96$ ), total content of ductile components ( $R^2=0.86, 0.95$ ), total clay mineral content comprising kaolinite, shale, and slate rock fragments ( $R^2=0.80, 0.92$ ), and mean grain size ( $R^2=0.63, 0.71$ ) when sample PW20 is rejected due to anomalous high Fe concentration and paleosol content (Fig. 10). Consequently,  $SiO_2/Al_2O_3$  ratios are positively correlated with total quartz content ( $R^2=0.76$ ), total detrital quartz content ( $R^2=0.76$ ), total content of ductile components ( $R^2=0.80$ ), total clay mineral content ( $R^2=0.68$ ) comprising kaolinite, shale and slate rock fragments, and mean grain size ( $R^2=0.79$ ) (Fig. 10). Correlation coefficients can be slightly increased up to  $R^2=0.83$  by selectively adding  $K_2O$ , Ca, and/or  $MgO$  on  $Al_2O_3$ . Similarly, Ba, Rb, and Sr show good to very good correlations with total quartz content ( $R^2=0.76, 0.75, 0.83$ ), total detrital quartz content ( $R^2=0.76, 0.75, 0.82$ ), total content of ductile components ( $R^2=0.77, 0.75, 0.83$ ), total clay mineral content comprising kaolinite, shale, and slate rock fragments ( $R^2=0.91, 0.91, 0.74$ ), and mean grain size ( $R^2=0.64, 0.61, 0.59$ ) (Fig. 11).

## Discussion

### Depositional environment

Different tectono-sedimentary phases are proposed for the intramontane Saar–Nahe basin ranging from Late Carboniferous proto-rift and pre-volcanic syn-rift to Permian volcanic syn-rift and post-rift phases (Henk 1993a; Stollhofen and Stanistreet 1994; Stollhofen 1998). In this study, the 1.72 m thick coal seam observed between 1767.82 and 1766.10 m (Fig. 1c–d) probably represents the coal seam Schwalbach, which determines the Stephanian A–B boundary (Bhardwaj 1955; Uhl and Jasper 2021). Thus, the rock sequence studied here belongs to the Stephanian A–B pre-volcanic syn-rift phase of the Saar–Nahe basin (Henk 1993a; Stollhofen and Stanistreet 1994; Stollhofen 1998). This is supported by the absence of igneous rock fragments and scarcity of feldspar

(two point counts in total), which is usually sourced from igneous rocks (Fig. 4b).

Published mineralogical data on Upper Carboniferous siliciclastic rocks from the Saar–Nahe basin report increasing feldspar contents over time beginning in the Stephanian (Schäfer 1989, 2011). This observation was interpreted as a change in the source area from the Rhenohercynian zone (i.e., Rhenish Massif) in the NW toward the Moldanubian zone (i.e., Black Forest, Vosges, Massif Central) in the S and SW (Schäfer 1989, 2011). The almost complete lack of feldspar observed in this study on Stephanian A–B deposits (i.e., litharenites and sub-litharenites in Fig. 4a) rather resembles the feldspar-poor compositions of Westphalian siliciclastic rocks (Schäfer 1989, 2011). Therefore, Westphalian and Stephanian A–B siliciclastic rocks had possibly the same source areas and the change in source area occurred in the Stephanian B or later. Alternatively, feldspar dissolution at depth may cause low feldspar contents (Blackbourn and Collinson 2022). However, the dominance of sedimentary and phyllitic rock fragments and the absence of feldspar-bearing plutonic rock fragments argue for a source effect. Moreover, even when depositional feldspar contents (detrital K-feldspar and plagioclase, authigenic minerals replacing K-feldspar and plagioclase, secondary porosity due to K-feldspar and plagioclase dissolution) are recalculated, contents are  $< 4\%$  indicating a feldspar-poor source area.

Fining upward cross-bedded fine to medium-grained sandstones, especially observed in the upper part of the section (Fig. 1d–e), are in accordance with previous sedimentological studies, which proposed fluvial deposition with prograding alluvial fans into the basin center (Stollhofen and Stanistreet 1994; Schäfer and Korsch 1998; Stollhofen 1998; Stollhofen et al. 1998; Schäfer 2011). Moreover, freshwater carbonate rocks typical for Late Carboniferous lacustrine environments within the intramontane Saar–Nahe basin (Stollhofen and Stanistreet 1994; Schäfer 2011) are absent in the section studied here. Small-scale coarsening upward sequences within large-scale fining upward sequences are interpreted as crevasse splays within the fluvial floodplains. Such depositional environments have also been suggested for other locations in the Saar–Nahe basin (Stollhofen and Stanistreet 1994; Stollhofen 1998; Stollhofen et al. 1998; Schäfer 2011). The floodplains are probably the areas where pedogenic features like paleosols formed and organic material deposited, which later formed coal seams.

The observation of convolute bedding, disrupted laminations, load casts, flame structures, and pseudo-nodules (Fig. 1d–e) indicates soft-sediment deformation. Soft-sediment deformation describes a rapid, near-surface process during which unlithified, water-saturated sedimentary strata are mobilized and original sedimentary structures may be altered (e.g., Allen 1977; Mills 1983; Owen 2003; Owen et al. 2011). Moreover, direct evidence of near-surface

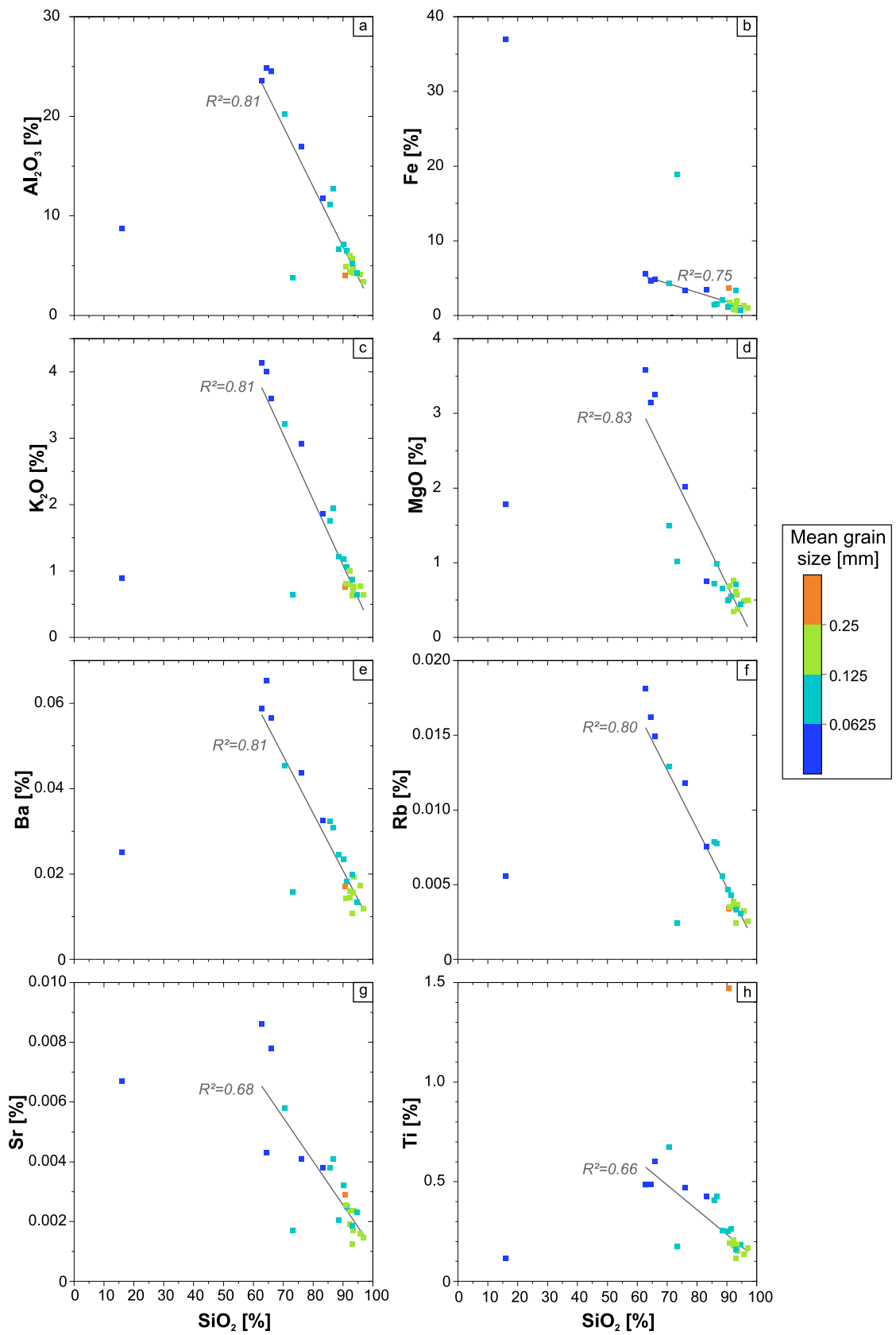


**Fig. 8** Harker variation diagrams based on pXRF whole-rock compositions. After exclusion of samples with anomalous Fe ( $\geq 19$  wt%) and Ti ( $\geq 1.5$  wt% and  $\leq 0.11$  wt%) concentrations, SiO<sub>2</sub> shows good to very good correlations with **a** Al<sub>2</sub>O<sub>3</sub> ( $R^2=0.81$ ), **b** Fe ( $R^2=0.75$ ), **c** K<sub>2</sub>O ( $R^2=0.81$ ), **d** MgO ( $R^2=0.83$ ), **e** Ba ( $R^2=0.81$ ), **f** Rb ( $R^2=0.80$ ), **g** Sr ( $R^2=0.68$ ), and **h** Ti ( $R^2=0.66$ ). Color code indicates mean grain size

deformation of unconsolidated sediment is given by an approximately 50 cm long undeformed root crosscutting the convolute bedding (Fig. 1e).

Soft-sediment deformation typically occurs in silt to fine sand deposits (Mills 1983), but has also been observed in coarser sandstones overlain by a less permeable sedimentary cover in close proximity to steep slopes (Postma 1983; Owen 2003). This may explain the occurrence of convolute bedding observed among coarse sandstones in this study, which are overlain by tight siltstones. Steep slopes may be related to cross-bedding or fault scarps due to normal fault activity during the syn-rift phase.

### Diagenetic sequence

The diagenetic processes of the sample set are subdivided into early-stage (i.e., eodiagenesis) and later stage (i.e., mesodiagenesis) characteristics (Foscolos et al. 1976; Burley et al. 1985). For this purpose, published burial curves and isotherms indicating Late Carboniferous to Early Permian maximum burial, Early Permian to Late Permian/Early Triassic uplift, and Late Permian/early Triassic to Late Jurassic renewed burial (Littke et al. 2000; Izart et al. 2016) are considered (Fig. 12).

Initial early-stage diagenesis involves near-surface processes after deposition under surface-like P–T conditions (Burley et al. 1985). This comprises the formation of paleosols of different mineralogical compositions such as siderite and calcite paleosol (Figs. 3e–f, 12). Ferruginous paleosols including siderite paleosols have been described for the Late Carboniferous in central Europe (e.g., Hampson et al. 1999; Fleck et al. 2001; Pearce et al. 2010; Opluštil et al. 2015, 2019) and are often spatially associated with coal deposits (Faure et al. 1995). Siderite paleosol typically forms in humid climates under reducing conditions in water-saturated soils (e.g., Mozley 1989; Browne and Kingston 1993; Faure et al. 1995; Ludvigson et al. 1998, 2013; Rosenau et al. 2013; Driese and Ober 2005; Letourmy et al. 2021). Therefore, siderite paleosol observed in this study is in accordance with the humid climatic conditions of the Stephanian (Roscher and Schneider 2006; Schäfer 2011). The presence of well-preserved euhedral siderite spherulites (Fig. 3e) points to an early-diagenetic near-surface formation process with little sedimentary overburden before the onset of significant mechanical compaction (Faure et al. 1995) (Fig. 12). The less-common calcite paleosol with textures similar to

rhizoliths are also early diagenetic products (Figs. 3f, 12), but contrasts the conditions indicated by siderite paleosol as they form in well-drained soils (Ludvigson et al. 2013; Rosenau et al. 2013). This may reflect the climatic changes from Stephanian humid to Rotliegend arid conditions or seasonal variations (Schäfer and Sneh 1983; Roscher and Schneider 2006; Schäfer 2011). Rather (semi-) arid conditions are also indicated by intercalated reddish sandstone layers that become more prominent toward the top (Fig. 1e).

In addition to paleosol formation, early-stage diagenesis also involves syn-depositional soft-sediment deformation (Figs. 3g, 12). It requires unconsolidated, water-saturated sediment and thus must have occurred in the shallow subsurface before significant mechanical compaction (Mills 1983; Owen 2003; Owen et al. 2011).

Some cleats are partially mineralized by syntaxial quartz cements indicating cleat formation before onset of or during quartz cementation (Figs. 3h, 12). In contrast, typically horizontal and non-mineralized fractures are probably related to unloading and thus represent induced structures (e.g., Holzhausen 1989).

With ongoing burial, the eodiagenesis transitions into mesodiagenesis involving chemical and mechanical compaction as well as dissolution processes. Mostly, rigid quartz grains are embedded in ductile components such as muscovite, slate, phyllite, and schist rock fragments, which deformed due to mechanical compaction (Fig. 3a). On occasion however, quartz overgrowth cements on quartz grains are in contact with ductile components pointing to the onset of quartz cementation before significant mechanical compaction initiated (Fig. 12). With the onset of mechanical compaction, detrital mica, clay- and muscovite-bearing rock fragments deformed in a ductile manner and were squeezed into the pore space resulting in a tighter rock fabric (Fig. 3a). Furthermore, point contacts between adjacent grains evolved into long, concavo-convex, and sutured contacts. This first burial phase peaked in Early Permian times and was followed by an uplift phase culminating in the Permian–Triassic boundary (Littke et al. 2000; Izart et al. 2016).

Kaolinite-filled pores formed by the dissolution of feldspar grains and rock fragments appear grain shaped (Figs. 3b, d, 12). This implies that the dissolution of feldspar grains and rock fragments and the subsequent formation of kaolinite took place after maximum burial and mechanical compaction reached during the Early Permian. If dissolution and kaolinite formation occurred prior to maximum compaction, secondary pores and/or kaolinite should show features of deformation, which is not observed here. As the intergranular-dissolution porosity is also only partially filled by calcite cements, this process occurred during burial diagenesis.

Chlorite replacing kaolinite (Fig. 3d) producing quartz and calcite as observed in some thin sections generally begins to form at temperatures  $> 120$  °C (Worden et al.

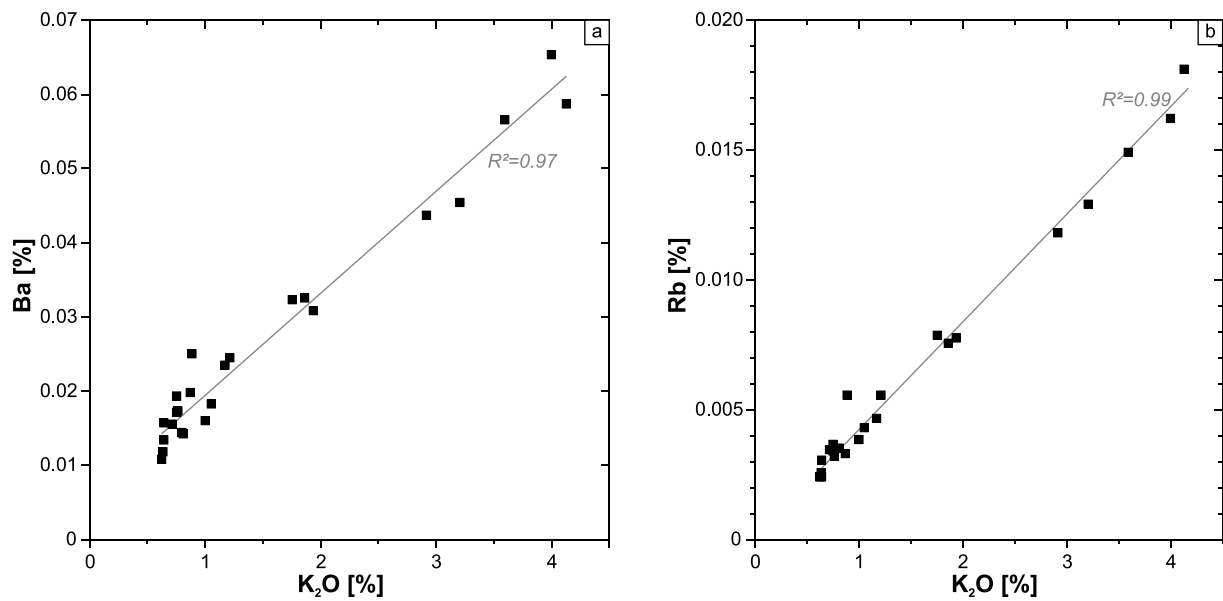


**Fig. 9** Correlations of **a** Ba ( $R^2=0.97$ ) and **b** Rb ( $R^2=0.99$ ) with  $K_2O$

2020 and references therein) and thus at higher temperatures than initial quartz cement formation at approximately 75 °C (Walderhaug 1994). Therefore, chloritization of kaolinite occurred after initial quartz cementation (Fig. 12). Moreover, the required temperatures > 120 °C were reached during the Permian burial peak and again during the Late Jurassic–Early Cretaceous reheating event (Littke et al. 2000; Izart et al. 2016). Since chloritization of kaolinite depends on the temporal onset of kaolinite formation that was placed after the Early Permian peak burial and after dissolution, the chloritization of kaolinite is probably associated with renewed subsidence and reheating between Early Triassic and mid Cretaceous times when the Stephanian A–B boundary exceeded the 120 °C isotherm again (Fig. 12). The iron required to form chlorite on the expense of kaolinite (Worden et al. 2020) may have been provided by the breakdown of pedogenic siderite. The breakdown of siderite was proposed to occur at temperatures > 120 °C (Worden et al. 2020) matching the temporal framework and temperature conditions proposed for chloritization. In contrast to chloritization of authigenic kaolinite, chloritization of rock fragments may have initiated slightly earlier.

The second, weaker burial phase from Late Permian to Late Jurassic accompanied by reheating and associated with chloritization also provides the required temperature conditions (75–150 °C) for a second quartz cementation phase. This is necessary to explain the interlocking grain contacts between authigenic quartz, calcite, and kaolinite, which have been locally observed (Fig. 3b) and cannot be placed before Early Permian peak burial because of grain-shaped dissolution features placed after mechanical compaction.

The calcite cements may have a Fe-rich core and a thin Fe-poor rim indicating depletion of Fe in the parental fluid during growth. The diagenetic sequence proposed here can be compared with published diagenetic sequences for other Late Carboniferous basins such as the Ouachita foreland basin (Walton et al. 1995), Ruhr basin (Greve et al. 2023, 2024), and present-day Lower Saxony basin (Wüstefeld et al. 2017a; Becker et al. 2017, 2019; Busch 2019). The different diagenetic sequences have in common that quartz cementation precedes mechanical compaction, although both may temporally overlap. However, differences in dissolution porosity and authigenic chlorite content may be related to different burial and uplift histories of the respective basins. Accordingly, the fault-controlled Saar–Nahe basin reveals higher subsidence rates, deeper burial, and thus higher diagenetic temperatures than the Variscan foreland basins (Littke et al. 1994, 2000; Bruns et al. 2013; Izart et al. 2016) whose subsidence is driven by the load of the Variscan fold and thrust belt causing lithospheric flexure (e.g., Opluštil and Cleal 2007). However, localized fault-controlled hydrothermal activity and uplift with surface exposure result in a further variation of the diagenetic sequence (Becker et al. 2017, 2019; Wüstefeld et al. 2017a, b). In general, higher temperatures increase diagenetic reaction rates (e.g., Trevena and Clark 1986; Lundegard 1992 and references therein).

### Reservoir quality

The sample set consistently reveals a tight texture dominated by rigid quartz grains and ductilely deformed components lacking porosity (Fig. 3). This qualitative petrographic

observation is supported by quantitative petrophysical data. Point-counted optical porosity underestimates porosity, possibly due to microporous minerals such as kaolinite (Hurst and Nadeau 1995). However, optical and measured porosity values show same order of magnitude. Based on low porosity < 7% and low permeability < 0.05 mD (Fig. 6), the sample set is consistently classified as tight (Smith et al. 2009). Published permeability data of coal (< 0.1 mD) and fractured coal (< 1 mD) samples from the Saar–Nahe basin (Durucan et al. 2004) are in accordance with permeability values of coal bearing samples (< 0.05 mD) presented in this study. Published porosity and permeability data for summarized Permo–Carboniferous lacustrine outcrop samples from the Saar–Nahe basin (Aretz et al. 2016) cover the same range of reservoir quality as presented in this study (< 10%, < 1 mD). Published porosity and permeability values of summarized Permo–Carboniferous eolian, alluvial, and fluvial outcrop samples (Aretz et al. 2016), however, exceed the values reported here by a few orders of magnitude. This may be due to the Permian red bed deposits and/or exposure and weathering in outcrop resulting in better reservoir qualities. Furthermore, Westphalian A–D samples from the Variscan foreland basin (Becker et al. 2017; Wüstefeld et al. 2017a; Busch et al. 2019; Greve et al. 2023, 2024; Quandt et al. 2022a) show higher maximum and mean porosity values than Stephanian A–B samples from the intramontane Saar–Nahe basin. Permeability values of the intramontane Saar–Nahe and foreland basins are comparable.

### Controls on reservoir quality

Porosity and permeability do not show a simple positive correlation with a single factor that controls reservoir quality (Fig. 7). Instead, an interplay of different factors is interpreted to control reservoir quality and porosity in particular. In contrast, permeability does not show any systematic correlation with petrographic features. The porosity controlling factors comprise (1) kaolinite, (2) quartz cement, (3) dissolution porosity, (4) IGV, (5) COPL and CEPL, (6) ductile components, (7) grain size, and (8) coal fragments in order of decreasing influence.

- (1) The highest porosity values are observed among samples with relative high authigenic kaolinite contents > 1%. Kaolinite is associated with dissolution porosity. The porous booklet-like microfabric probably preserved some secondary porosity (Figs. 3d, 7a). In contrast, authigenic carbonate minerals precipitated in pore space, but are not characterized by intragranular porosity (Fig. 3b) and thus reduced porosity to a larger degree.
- (2) Samples with relatively high syntaxial quartz cement contents > 2% show the highest porosity (Figs. 3c, 7b).

Syntaxial quartz cement is interpreted as an early stage diagenetic phase. Therefore, quartz cements probably stabilized the grain framework and thus preserved primary porosity. Similar conclusions were made on Early Triassic red beds (i.e., Buntsandstein/Bunter) from southwest Germany (Quandt et al. 2022b).

- (3) The highest porosity values are observed among samples with > 2% intragranular porosity due to dissolution of feldspar and rock fragments (Figs. 3d, 7c). Thus, the secondary pore space remained open without any significant authigenic cementation.
- (4) The IGV represents an indicator of chemical and mechanical compaction (Paxton et al. 2002). With increasing IGV, porosity increases (Fig. 7d).
- (5) In accordance with observed positive correlations of authigenic quartz and kaolinite with porosity, the highest porosity values are observed among samples with high CEPL values (Fig. 7f). This is due to the reservoir quality preserving effects explained in (1) and (2) since CEPL is a function of pore-filling cements among others. Consequently, an increase in COPL values due to mechanical compaction reduces porosity (Fig. 7e).
- (6) With an increase in the content of ductile components, porosity decreases (Fig. 7g). This reflects the qualitative, petrographic observation that ductile components were squeezed into the pore space due to mechanical compaction reducing porosity (Fig. 3a).
- (7) Samples with larger mean grain sizes show better porosity than samples with smaller mean grain sizes (Fig. 7h). Grain size in turn is a function of total detrital quartz content and content of ductile components (Fig. 4a). Thus, mean grain size and detrital quartz content are positively correlated.
- (8) Samples bearing coal fragments are frequently associated with incompletely or non-sealed natural cleats (Fig. 3h). This qualitative observation implies an increase in reservoir quality, which is not well substantiated by quantitative data (Fig. 7i). Therefore, this may be a local effect.

Similarly, a range of factors were proposed to control reservoir quality of the Variscan foreland basin rock successions. They include grain size, pore-filling cement content, content of ductile components, and dissolution porosity (Busch et al. 2019; Quandt et al. 2022a; Greve et al. 2024). As in the Saar–Nahe basin, they particularly exert an influence on porosity. In contrast, permeability is rather unaffected by these factors.

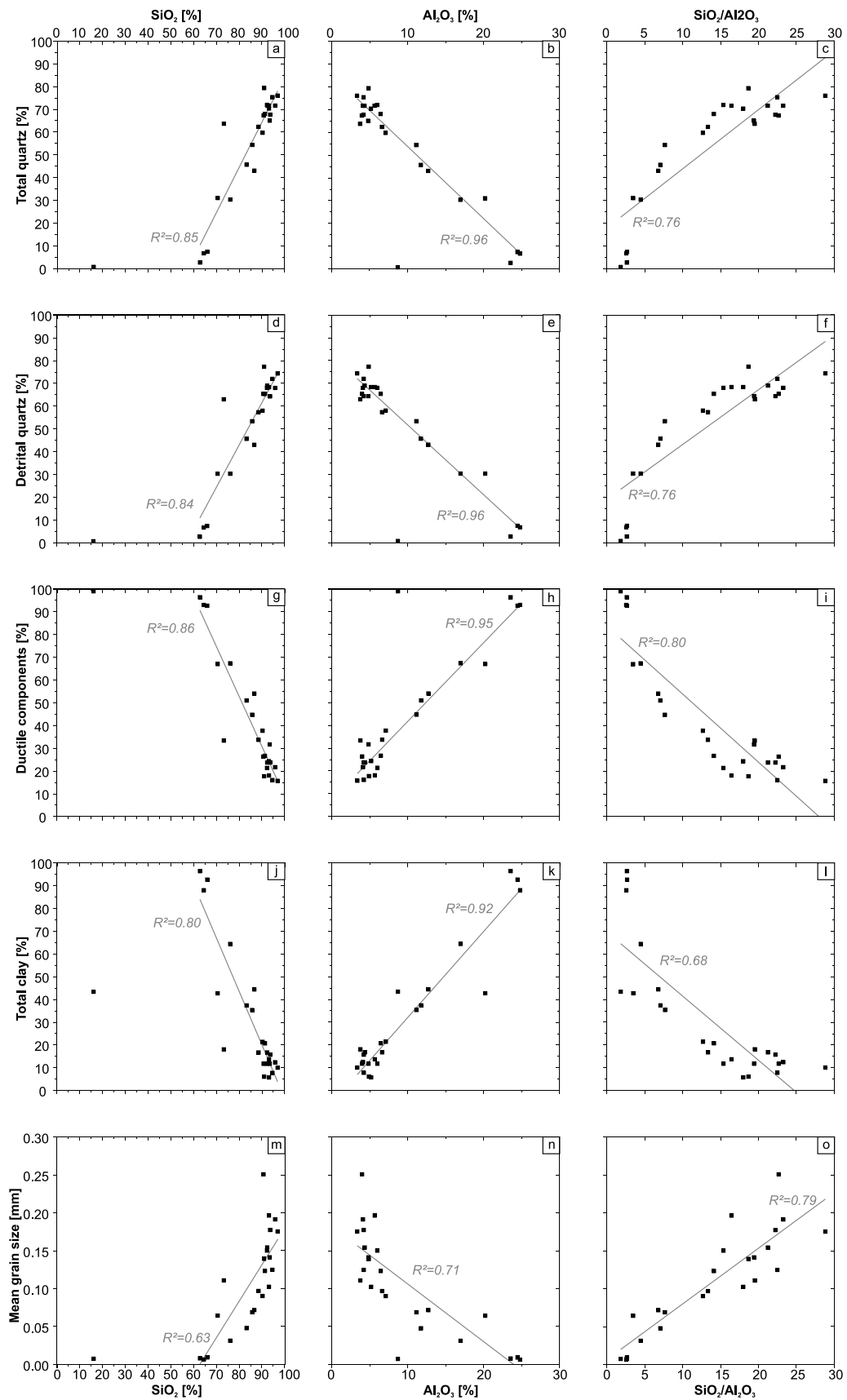


**Fig. 10** Correlations of  $\text{SiO}_2$ ,  $\text{Al}_2\text{O}_3$ , and  $\text{SiO}_2/\text{Al}_2\text{O}_3$  with **a–c** total quartz content comprising detritus and cement ( $R^2=0.85, 0.96, 0.76$ ), **d–f** detrital quartz content ( $R^2=0.84, 0.96, 0.76$ ), **g–i** total content of ductile components ( $R^2=0.86, 0.95, 0.80$ ), **j–l** total clay mineral content comprising authigenic kaolinite, slate and shale rock fragments ( $R^2=0.80, 0.92, 0.68$ ), and **m–o** mean grain size ( $R^2=0.63, 0.71, 0.79$ ). Outliers with anomalous high Fe ( $\geq 19$  wt%) concentrations have been partly excluded for  $R^2$  calculation

### Applicability and utility of pXRF data and implications for sandstone geochemistry

Since the first commercially available devices in the 1980s, pXRF have been refined and are increasingly used in science and industry (e.g., Young et al. 2016; Ryan et al. 2017; Gallhofer and Lottermoser 2018; Lemiere 2018). The pXRF data collected in this study have been evaluated with petrographic point counting data. The observed correlations ( $R^2$  up to 0.96) between geochemistry and mineralogy (Figs. 10, 11) suggest reliable pXRF data. In detail,  $\text{SiO}_2/\text{Al}_2\text{O}_3$  ratios based on pXRF-measured  $\text{SiO}_2$  and  $\text{Al}_2\text{O}_3$  concentrations provide an estimate on relative quartz and clay contents in a rock sample (Fig. 10c, f, l). Since quartz and clay contents correlate with mean grain size,  $\text{SiO}_2/\text{Al}_2\text{O}_3$  ratios consequently enable the derivation of the relative mean grain size (Fig. 10o). Similarly, the Ba, Rb, and Sr concentrations show correlations with quartz content, clay content, and mean grain size (Fig. 11a–f, j–o). Therefore, pXRF analyzers represent a rapid alternative to laboratory XRF set-ups to in-situ measure large rock sample sets, rock outcrops, or cutting material in case drill core material is not available without the necessity for sample preparation.

The correlations are largely due to the geochemical purity of quartz ( $\text{SiO}_2$ ) and due to aluminum being a constituent of feldspars and all phyllosilicates such as illite, kaolinite, and muscovite as prominent rock forming minerals (Herron 1988; Pearce et al. 2005, 2010; Svendsen et al. 2007; Götze et al. 2021). Similarly, Ba, Rb, and Sr concentrations of the samples studied here are controlled by mica and clay minerals such as muscovite and illite. Very good correlations of Ba ( $R^2=0.97$ ) and Rb ( $R^2=0.99$ ) with  $\text{K}_2\text{O}$  indicate substitution for K in detrital muscovite and muscovite-bearing rock fragments (e.g., Tischendorf et al. 2007). However, Ba concentrations have to be interpreted with care due to the potential use of barite-bearing additives in drilling fluids (Pearce et al. 2010). Furthermore, sandstones richer in carbonate cements may have elevated Sr concentrations due to carbonate minerals (Pearce et al. 2010).

The derivation of mineralogy and grain size from pXRF measurements may require some data processing such as rejecting samples with anomalous high Fe contents. However, data processing can be avoided when the  $\text{SiO}_2/\text{Al}_2\text{O}_3$  ratio is used instead of  $\text{SiO}_2$  or  $\text{Al}_2\text{O}_3$  concentrations alone by which the effect of anomalous geochemical compositions

is attenuated. In turn, relative high Fe contents may be used to detect siderite paleosols within sandstone sample sets.

### Implications for mine flooding and coalbed methane extraction

Among others, mine water rebound is a function of porosity and permeability of the subsurface including rock matrix, fractures, and mine workings. With porosity and permeability values  $< 10\%$  and  $< 1$  mD, respectively, the reservoir quality of the analyzed section is poor. In addition, non-mineralized fractures are induced structures due to unloading and are not expected to be present in the subsurface rock volume. Therefore, it is suggested that mine workings such as shafts and galleries are the main contributors to mine water rebound as also pointed out for the German Ruhr and Ibbenbüren hard coal districts (Allgaier et al. 2022; Greve et al. 2023; Quandt et al. 2022a). Similarly, potential geothermal applications would be restricted to mine workings and permeable faults. With progressive mine flooding, mine water will also permeate the rock column surrounding the mine workings and thus changing the local pore pressure regime. For simulations attempting to model the resulting ground movement, the heterogeneity of the subsurface rock volume shown in this study needs to be taken into account. This also involves overlying Autunian strata, which are characterized by changing depositional environments and climatic conditions pointing to an even more heterogeneous geological architecture in terms of facies and resulting rock properties.

Moreover, the Lorraine-Saar basin has been studied in terms of its coalbed methane reservoir potential with a focus on cleats (Izart et al. 2016; Privalov et al. 2020). In coalbed methane reservoirs, reservoir volume is determined by pores and cleats, i.e., mostly opening-mode fractures in coal. In contrast to conventional gas plays, methane is adsorbed on the coal surface. Therefore, the pore surface area is an important measure for coalbed methane reservoir quality (Laubach et al. 1998; Moore 2012). Coalbed methane may be replaced by injecting  $\text{CO}_2$  (i.e., carbon capture and storage) (e.g., Kalkreuth et al. 2013).

This study provides a qualitative understanding to which extend cleats are sealed by secondary mineralization. The microscopic features studied here are restricted to cleats crosscutting up to millimeter-thick coal seams and coal fragments. However, macroscopic cleats crosscutting the meter-thick Schwalbach coal seams are also observed. The cleats observed in this study are oriented parallel (i.e., horizontal) and normal (i.e., vertical) to the bedding-parallel coal fragments. Horizontal cleats are typically open and may be related to unloading effects (Holzhausen 1989) and are probably absent in the subsurface under reservoir conditions. Some vertical cleats are partially or completely sealed

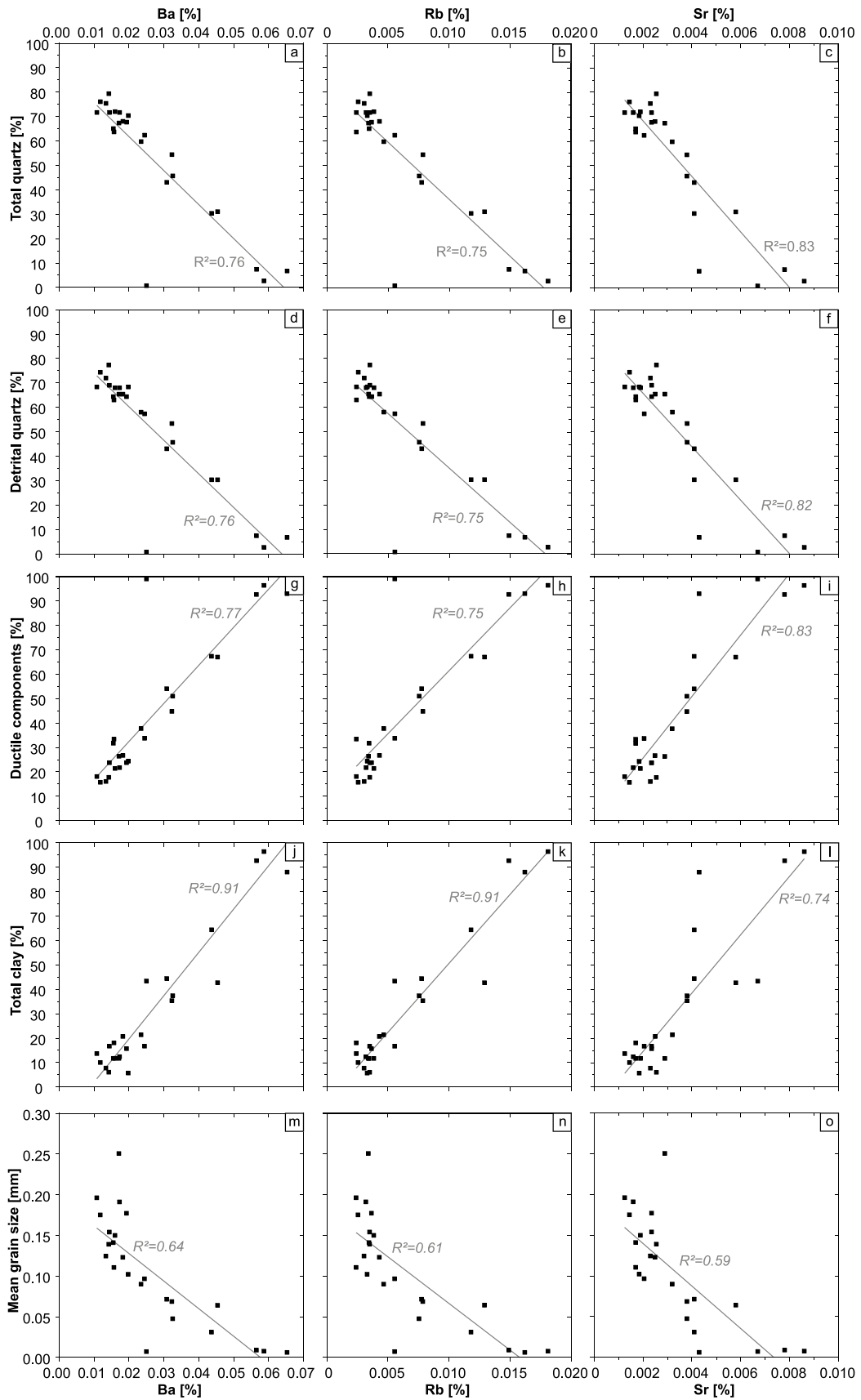


**Fig. 11** Correlations of Ba, Rb, and Sr with **a–c** total quartz content comprising detritus and cement ( $R^2=0.76, 0.75, 0.83$ ), **d–f** detrital quartz content ( $R^2=0.76, 0.75, 0.82$ ), **g–i** total content of ductile components ( $R^2=0.77, 0.75, 0.83$ ), **j–l** total clay mineral content comprising authigenic kaolinite, slate and shale rock fragments ( $R^2=0.91, 0.91, 0.74$ ), and **m–o** mean grain size ( $R^2=0.64, 0.61, 0.59$ )

with quartz or Fe-rich carbonate cements. The latter may show multiple host rock-parallel inclusion bands indicating repeated crack and sealing events (Hilgers and Urai 2002) or an oscillation process (Wiltshcko and Morse 2001; Hilgers and Urai 2005). This implies that cleats must have been present during quartz and Fe-carbonate cementation. Cleats may have formed during early diagenesis or during progressive burial, possibly until a temperature of approximately 75 °C was reached and quartz cementation initiated. As a result, cleat-filling minerals reduce the cleat surface and thus deteriorate coalbed methane reservoir quality. The bonding of vein cement in coal horizons, however, may control induced refracturing (Virgo et al. 2014).

Furthermore, spherulitic siderite occurs within coal fragments and formed during early diagenesis. Since early-diagenetic euhedrally developed siderite spherulites are undeformed and syntaxial quartz cement represent only a partial infill of cleats leaving some porosity, cleat-related

porosity may have been preserved during burial. Completely sealed cleats in contrast probably reduce reservoir quality. However, samples bearing coal fragments associated with cleats do not show any systematic enhancement of reservoir quality. Therefore, the effect of cleat mineralization on coalbed methane reservoir potential remains inconclusive, but a deteriorating effect of authigenic cementation on reservoir quality is suggested based on qualitative observations. These microscopic observations on cleats make aware of the possibility of complete and incomplete cleat sealing. In studies focusing on large-scale cleats in meter-thick coal seams, microtextures and secondary mineralization of cleats need to be considered to evaluate coalbed methane potentials.

### Conclusion

The siliciclastic rock section shows large-scale fining upward sequences in agreement with deposition in a river channel. Intercalated small-scale coarsening upward sequences indicate crevasse splays along a floodplain that is characterized by soft-sediment deformation and sideritic paleosol formation under a humid climate. Calcitic paleosols and reddish sandstone layers possibly adumbrate the beginning climate change toward the arid Rotliegend. The detrital mineralogy lacking igneous rock fragments and feldspar is in accordance

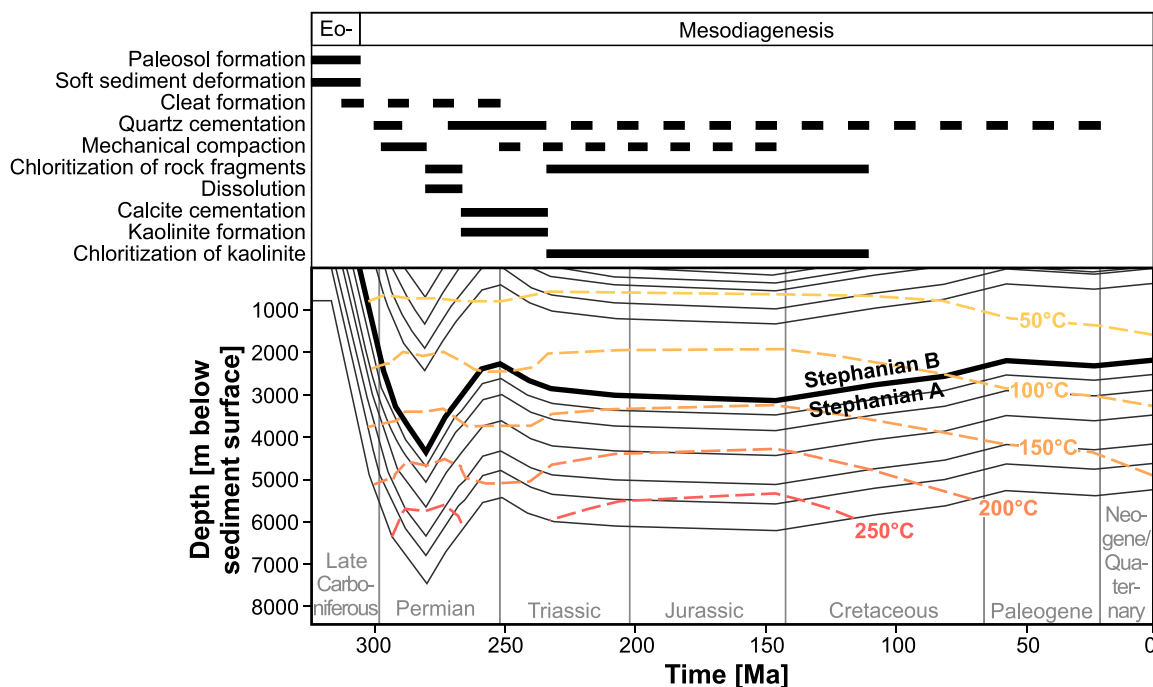


**Fig. 12** Diagenetic sequence of the sample set in comparison with published burial curves and associated isotherms for the Saar–Nahe basin (modified after Littke et al. 2000). The sample set stratigraphically covers the Stephanian A–B boundary. The diagenetic sequence is established considering the relative sequence of diagenetic phases

inferred from microscopic analyses and the temperature conditions at which these diagenetic phases are stable using the 50–250 °C isotherms proposed by Littke et al. (2000). Dotted lines indicate uncertainty

with the Stephanian A–B pre-volcanic syn-rift phase of the Saar–Nahe basin.

With permeability and porosity values  $< 0.05$  mD and  $< 7\%$ , respectively, reservoir quality is consistently poor. Porosity is controlled by an interplay of different factors, whereas permeability shows no systematic variation with any petrographic feature. Syntaxial quartz cements stabilizing the grain framework against mechanical compaction preserved primary porosity. In addition, dissolution of feldspar and rock fragments forming secondary porosity and partly replaced by microporous kaolinite also enhanced porosity. In contrast, mechanical compaction postdating the onset of quartz cementation and local carbonate cements reduced porosity. Compaction porosity loss dominates over cementation porosity loss and is reflected by a tight grain framework with ductilely deformed phyllosilicates squeezed into pore space.

The  $\text{SiO}_2/\text{Al}_2\text{O}_3$  ratios and Ba, Rb, and Sr concentrations of the feldspar-free and carbonate-poor sandstones measured with a pXRF analyzer enable a first-order estimation of relative grain size, quartz content, and phyllosilicate content. Thus, the pXRF workflow provides a rapid in-situ determination of whole-rock geochemical composition of a rock sample from which mineralogical and textural rock parameters can be approximately inferred. The pXRF does not require sample preparation and may be applied on cutting material in case no drill core material is available. In how far this conclusion can be transferred to rock sequences with differing mineralogical composition needs to be tested.

With regard to post-mining in the Saar hard coal district, mine water rebound focuses on the open mine workings, whereas the rock volume is tight except where non-mineralized fractures are open and connected within the current stress regime. Qualitative macroscopic core logging, however, suggest that most fractures are mineralized and thus do not significantly contribute to the mine water rebound. With ongoing time of mine flooding, however, mine water will slowly permeate the rock volume. Regarding the potential of coalbed methane, the observation of minerals partially or completely sealing cleats needs to be considered.

**Supplementary Information** The online version contains supplementary material available at <https://doi.org/10.1007/s00531-024-02394-x>.

**Acknowledgements** This work was undertaken in the framework of the project FloodRisk (03G0893A) funded by the Federal Ministry of Education and Research, Germany. We thank the Geological Survey North-Rhine-Westphalia for the access to the drill core Primsweiler-1 and the permission to log and sample it. Thin sections were thankfully prepared by Martin von Dollen at the Institute of Structural Geology and Tectonics, Institute of Applied Geosciences, Karlsruhe Institute of Technology. We are thankful to Vaibhav Jaiswal and Chinmaya Behera for their help in the laboratory. We thank Graham Blackburn and an anonymous reviewer for their constructive comments that helped to improve the manuscript. We also thank guest editor Jan

Schwarzbauer and editor-in-chief Ulrich Riller for editorial handling of the manuscript.

**Author contributions** Conceptualization: DQ. Methodology: BB. Formal analysis and investigation: DQ. Visualization: DQ. Writing — original draft and preparation: DQ. Writing — review and editing: DQ, BB, JG, CH. Funding acquisition: CH, BB. Resources: JG, BB. Project administration: DQ.

**Funding** Open Access funding enabled and organized by Projekt DEAL. This work was undertaken in the framework of the project FloodRisk (03G0893A) funded by the Federal Ministry of Education and Research, Germany.

**Data availability** All data presented in this article is available as appendix in the Online Resources.

## Declarations

**Conflict of interest** The authors declare that they have no known competing financial interests or personal relationships that could have appeared to influence the work reported in this paper.

**Open Access** This article is licensed under a Creative Commons Attribution 4.0 International License, which permits use, sharing, adaptation, distribution and reproduction in any medium or format, as long as you give appropriate credit to the original author(s) and the source, provide a link to the Creative Commons licence, and indicate if changes were made. The images or other third party material in this article are included in the article's Creative Commons licence, unless indicated otherwise in a credit line to the material. If material is not included in the article's Creative Commons licence and your intended use is not permitted by statutory regulation or exceeds the permitted use, you will need to obtain permission directly from the copyright holder. To view a copy of this licence, visit <http://creativecommons.org/licenses/by/4.0/>.

## References

- Ajdkiewicz JM, Lander RH (2010) Sandstone reservoir quality prediction: the state of the art. *AAPG Bull* 94(8):1083–1091
- Alber M, Fritsch R (2011) Rock mechanical analysis of a ML = 4.0 seismic event induced by mining in the Saar District, Germany. *Geophys J Int* 186(1):359–372
- Allen JR (1977) The possible mechanics of convolute lamination in graded sand beds. *J Geol Soc* 134(1):19–31
- Allgaier F, Busch B, Niederhuber T, Quandt D, Müller B, Hilgers C (2022) Fracture network characterisation of the naturally fractured upper carboniferous sandstones combining outcrop and wellbore data, Ruhr Basin, Germany. *Zeitschrift Der Deutschen Gesellschaft Für Geowissenschaften* 173(4):599–623
- Anderle HJ (1987) The evolution of the South Hunsrück and Taunus borderzone. *Tectonophysics* 137(1–4):101–114
- Aretz A, Bär K, Götz AE, Sass I (2016) Outcrop analogue study of Permocarbiniferous geothermal sandstone reservoir formations (northern Upper Rhine Graben, Germany): impact of mineral content, depositional environment and diagenesis on petrophysical properties. *Int J Earth Sci* 105:1431–1452
- Becker I, Wüstefeld P, Koehrer B, Felder M, Hilgers C (2017) Porosity and permeability variations in a tight gas sandstone reservoir analogue, Westphalian D, Lower Saxony Basin, NW Germany: influence of depositional setting and diagenesis. *J Pet Geol* 40(4):363–389

- Becker I, Busch B, Koehrer B, Adelmann D, Hilgers C (2019) Reservoir quality evolution of upper carboniferous (Westphalian) tight gas sandstones, lower Saxony Basin, NW Germany. *J Pet Geol* 42(4):371–392
- Bhardwaj DC (1955) The spore genera from the upper carboniferous coal of the Saar and their value in stratigraphical studies. *J Palaeosci* 4:119–149
- Bischoff M, Cete A, Fritschen R, Meier T (2010) Coal mining induced seismicity in the Ruhr area, Germany. *Pure Appl Geophys* 167(1):63–75
- Bjørlykke K, Jahren J (2012) Open or closed geochemical systems during diagenesis in sedimentary basins: constraints on mass transfer during diagenesis and the prediction of porosity in sandstone and carbonate reservoirs. *AAPG Bull* 96(12):2193–2214
- Blackbourn GA, Collinson JD (2022) Quartzitic sandstones in the Namurian and lower Westphalian succession of the southern North Sea: a new high-permeability Carboniferous reservoir type. *J Pet Geol* 45(4):363–393
- Bloch S (1991) Empirical prediction of porosity and permeability in sandstones. *AAPG Bull* 75(7):1145–1160
- Brix MR, Drozdowski G, Greiling RO, Wolf R, Wrede V (1988) The N Variscan margin of the Ruhr coal district (Western Germany): structural style of a buried thrust front? *Geol Rundsch* 77:115–126
- Browne GH, Kingston DM (1993) Early diagenetic spherulitic siderites from Pennsylvanian palaeosols in the boss point formation, Maritime Canada. *Sedimentology* 40:461–474
- Bruns B, Di Primio R, Berner U, Littke R (2013) Petroleum system evolution in the inverted Lower Saxony Basin, northwest Germany: a 3 D basin modeling study. *Geofluids* 13(2):246–271
- Bungart R, Hüttl RF (2001) Production of biomass for energy in post-mining landscapes and nutrient dynamics. *Biomass Bioenerg* 20(3):181–187
- Burley SD, Kantorowicz JD, Waugh B (1985) Clastic diagenesis. *Geol Soc* 18(1):189–226
- Busch B, Becker I, Koehrer B, Adelmann D, Hilgers C (2019) Porosity evolution of two upper carboniferous tight-gas-fluvial sandstone reservoirs: impact of fractures and total cement volumes on reservoir quality. *Mar Pet Geol* 100:376–390
- Busch B, Hilgers C, Adelmann D (2020) Reservoir quality controls on Rotliegend fluvio-aeolian wells in Germany and the Netherlands, Southern Permian Basin-impact of grain coatings and cements. *Mar Pet Geol* 112:104075
- Busch B, Adelmann D, Herrmann R, Hilgers C (2022a) Controls on compactional behavior and reservoir quality in a Triassic Buntsandstein reservoir, Upper Rhine Graben, SW Germany. *Mar Petrol Geol* 136:105437
- Busch B, Spitzner AD, Adelmann D, Hilgers C (2022b) The significance of outcrop analog data for reservoir quality assessment: a comparative case study of Lower Triassic Buntsandstein sandstones in the Upper Rhine Graben. *Mar Pet Geol* 141:105701
- Busch A, Krooss BM, Kempka T, Waschbusch M, Fernández-Steeger T, Schluter R (2009) Carbon dioxide storage in abandoned coal mines. In: Grobe M, Pashin JC, Dodge RL (eds) Carbon dioxide sequestration in geological media—state of the science. *AAPG Studies in Geology*, pp 643–653
- Cleal CJ, Opluštil S, Thomas BA, Tenchov Y, Abbink OA, Bek J, Dimitrova T, Drábková J, Hartkopf-Fröder C, van Hoof T, Kędzior A, Jarzembowski E, Jasper K, Libertin M, McLean D, Oliwkiewicz-Miklasinska M, Pšenička J, Ptak B, Schneider JW, Schultka S, Šimůnek Z, Uhl D, Waksmondzka MI, van Waveren I, Zdroew EL (2009) Late Moscovian terrestrial biotas and palaeoenvironments of Variscan Euramerica. *Neth J Geosci* 88(4):181–278
- Declercq PY, Dusar M, Pirard E, Verbeurgt J, Choopani A, Devleeschouwer X (2023) Post mining ground deformations transition related to coal mines closure in the campine coal basin, Belgium, evidenced by three decades of MT-InSAR data. *Remote Sens* 15(3):725
- Deutsche Stratigraphische Kommission (2016) Stratigraphische Tabelle von Deutschland 2016, Menning M, Hendrich, A (eds) *Geoforschungszentrum Potsdam*
- Driese SG, Ober EG (2005) Paleopedologic and paleohydrologic records of precipitation seasonality from Early Pennsylvanian "underclay" paleosols, USA. *J Sediment Res* 75(6):997–1010
- Durucan S, Shi JQ, Korre A (2004) Numerical modelling and prediction of abandoned mine methane recovery: field application at the Saar coalfield, Germany. *Geol Belgica* 7(3–4):207–213
- Everingham JA, Svobodova K, Lèbre È, Owen JR, Worden S (2022) Comparative capacity of global mining regions to transition to a post-mining future. *Extract Ind Soc* 11:101136
- Faure K, Harris C, Willis JP (1995) A profound meteoric water influence on genesis in the Permian Waterberg Coalfield, South Africa; evidence from stable isotopes. *J Sediment Res* 65(4a):605–613
- Fleck S, Michels R, Izart A, Elie M, Landais P (2001) Palaeoenvironmental assessment of Westphalian fluvio-lacustrine deposits of Lorraine (France) using a combination of organic geochemistry and sedimentology. *Int J Coal Geol* 48(1–2):65–88
- Folk RL (1980) *Petrology of sedimentary rocks*. Hemphill publishing company, Austin
- Folk RL, Ward WC (1957) Brazos River bar [Texas], a study in the significance of grain size parameters. *J Sediment Res* 27(1):3–26
- Foscolos AE, Powell TG, Gunther PR (1976) The use of clay minerals and inorganic and organic geochemical indicators for evaluating the degree of diagenesis and oil generating potential of shales. *Geochim Cosmochim Acta* 40(8):953–966
- Gallhofer D, Lottermoser BG (2018) The influence of spectral interferences on critical element determination with portable X-ray fluorescence (pXRF). *Minerals* 8(8):320
- Götze J, Pan Y, Müller A (2021) Mineralogy and mineral chemistry of quartz: a review. *Mineral Mag* 85(5):639–664
- Greve J, Busch B, Quandt D, Knaak M, Hartkopf-Fröder C, Hilgers C (2023) Coupling heat conductivity and lithofacies of the coal-bearing upper carboniferous in the eastern Ruhr Basin, NW Germany. *Zeitschrift Der Deutschen Gesellschaft Für Geowissenschaften* 173(4):673–695
- Greve J, Busch B, Quandt D, Knaak M, Hilgers C (2024) The influence of sedimentary facies, mineralogy, and diagenesis on reservoir properties of the coal-bearing upper carboniferous of NW Germany. *Petrol Geosci* 30:2023
- Hampson G, Stollhofen H, Flint S (1999) A sequence stratigraphic model for the lower coal measures (upper carboniferous) of the Ruhr district, north-west Germany. *Sedimentology* 46(6):1199–1231
- Henk A (1993a) Late orogenic basin evolution in the Variscan Inter-nides: the Saar–Nahe Basin, southwest Germany. *Tectonophysics* 223(3–4):273–290
- Henk A (1993b) Subsidenz und Tektonik des Saar-Nahe-Beckens (SW-Deutschland). *Geol Rundsch* 82(1):3–19
- Herron MM (1988) Geochemical classification of terrigenous sands and shales from core or log data. *J Sediment Res* 58(5):820–829
- Hertle M, Littke R (2000) Coalification pattern and thermal modelling of the Permo-Carboniferous Saar Basin (SW-Germany). *Int J Coal Geol* 42(4):273–296
- Hilgers C, Urai JL (2002) Microstructural observations on natural syntectonic fibrous veins: implications for the growth process. *Tectonophysics* 352(3–4):257–274
- Hilgers C, Urai JL (2005) On the arrangement of solid inclusions in fibrous veins and the role of the crack-seal mechanism. *J Struct Geol* 27(3):481–494

- Holzhausen GR (1989) Origin of sheet structure, 1. Morphology and boundary conditions. *Eng Geol* 27(1–4):225–278
- Hurst A, Nadeau PH (1995) Clay microporosity in reservoir sandstones: an application of quantitative electron microscopy in petrophysical evaluation. *AAPG Bull* 79(4):563–573
- Ingersoll RV, Bullard TF, Ford RL, Grimm JP, Pickle JD, Sares SW (1984) The effect of grain size on detrital modes: a test of the Gazzi-Dickinson point-counting method. *J Sediment Res* 54(1):103–116
- Izart A, Barbarand J, Michels R, Privalov VA (2016) Modelling of the thermal history of the Carboniferous Lorraine Coal Basin: consequences for coal bed methane. *Int J Coal Geol* 168:253–274
- Juch D, Roos WF, Wolff M (1994) Kohleninhaltsfassung in den westdeutschen Steinkohlenlagerstätten. In: Drozdowski G, Juch D, Lommerzheim AJ, Roos WF, Wolff M, Wrede V (eds) *Das Subvariscikum Nordwestdeutschlands*. *Fortschr Geol Rheinld U Westf* 38:189–307
- Kalkreuth W, Holz M, Levandowski J, Kern M, Casagrande J, Weniger P, Krooss B (2013) The coalbed methane (CBM) potential and CO<sub>2</sub> storage capacity of the Santa Terezinha Coalfield, Paraná Basin, Brazil—3D modelling, and coal and carbonaceous shale characteristics and related desorption and adsorption capacities in samples from exploration borehole CBM001-ST-RS. *Energy Explor Exploit* 31(4):485–527
- Klinkenberg LJ (1941) The permeability of porous media to liquids and gases drilling and production practice. American Petroleum Institute, Washington DC, pp 200–213
- Konicek P, Jirankova E, Kajzar V, Schreiber J, Malucha P, Schuchova K (2022) Seismic activity and flooding of hard coal mines in the Ostrava–Karvina coalfield. *J Sustain Min* 21(4):249–260
- Korsch RJ, Schäfer A (1991) Geological interpretation of DEKORP deep seismic reflection profiles 1C and 9N across the variscan Saar–Nahe Basin southwest Germany. *Tectonophysics* 191(1–2):127–146
- Korsch RJ, Schäfer A (1995) The Permo-Carboniferous Saar–Nahe Basin, south-west Germany and north-east France: basin formation and deformation in a strike-slip regime. *Geol Rundsch* 84(2):293–318
- Laubach SE, Marrett RA, Olson JE, Scott AR (1998) Characteristics and origins of coal cleat: a review. *Int J Coal Geol* 35(1–4):175–207
- Lemiere B (2018) A review of pXRF (field portable X-ray fluorescence) applications for applied geochemistry. *J Geochem Explor* 188:350–363
- Letourmy Y, Driese SG, Sims JR (2021) Absence of evidence of climate-driven cycles in Carboniferous deposits of Joggins, Nova Scotia, Canada: influence of salt withdrawal tectonics on deposition and pedogenesis. *J Sediment Res* 91(2):167–185
- Litke R, Büker C, Lückge A, Sachsenhofer RF, Welte DH (1994) A new evaluation of palaeo-heat flows and eroded thicknesses for the Carboniferous Ruhr basin, western Germany. *Int J Coal Geol* 26(3–4):155–183
- Litke R, Büker C, Hertle M, Karg H, Stroetmann-Heinen V, Oncken O (2000) Heat flow evolution, subsidence and erosion in the Rheno-Hercynian orogenic wedge of central Europe. *Geol Soc* 179(1):231–255
- Ludvigson GA, González LA, Metzger RA, Witzke BJ, Brenner RL, Murillo AP, White TS (1998) Meteoric sphaerosiderite lines and their use for paleohydrology and paleoclimatology. *Geology* 26(11):1039–1042
- Ludvigson GA, González LA, Fowle DA, Roberts JA, Driese SG, Villarreal MA, Smith JJ, Suarez MB (2013) Paleoclimatic applications and modern process studies of pedogenic siderite. *SEPM* 104:79–87
- Lundegard PD (1992) Sandstone porosity loss; a "big picture" view of the importance of compaction. *J Sediment Res* 62(2):250–260
- Meissner R, Bartelsen H, Murawski H (1980) Seismic reflection and refraction studies for investigating fault zones along the Geotraverse Rhenohertzynikum. *Tectonophysics* 64(1–2):59–84
- Meissner R, Springer M, Flüh E (1984) Tectonics of the Variscides in North-Western Germany based on seismic reflection measurements. *Geol Soc* 14(1):23–32
- Menéndez J, Ordóñez A, Álvarez R, Loredo J (2019) Energy from closed mines: underground energy storage and geothermal applications. *Renew Sustain Energy Rev* 108:498–512
- Meschede M (2018) *Geologie Deutschlands: Ein prozessorientierter Ansatz*, 2nd edn. Springer-Verlag, Berlin
- Mills PC (1983) Genesis and diagnostic value of soft-sediment deformation structures—a review. *Sed Geol* 35(2):83–104
- Moore TA (2012) Coalbed methane: a review. *Int J Coal Geol* 101:36–81
- Morad S, Al-Ramadan K, Ketzer JM, De Ros LF (2010) The impact of diagenesis on the heterogeneity of sandstone reservoirs: a review of the role of depositional facies and sequence stratigraphy. *AAPG Bull* 94(8):1267–1309
- Morad S, Ketzer M, de Ros LF (2012) Linking diagenesis to sequence stratigraphy. Wiley-Blackwell, West Sussex
- Mozley PS (1989) Relation between depositional environment and the elemental composition of early diagenetic siderite. *Geology* 17(8):704–706
- Opluštil S, Cleal CJ (2007) A comparative analysis of some Late Carboniferous basins of Variscan Europe. *Geol Mag* 144(3):417–448
- Opluštil S, Lojka R, Rosenau NA, Strnad L, Sýkorová I (2015) Middle Moscovian climate of eastern equatorial Pangea recorded in paleosols and fluvial architecture. *Palaeogeogr Palaeoclimatol Palaeoecol* 440:328–352
- Opluštil S, Lojka R, Rosenau N, Strnad L, Kędzior A (2019) Climatically-driven cyclicity and peat formation in fluvial setting of the Moscovian-Early Kasimovian Cracow Sandstone Series, Upper Silesia (Poland). *Int J Coal Geol* 212:103234
- Owen G (2003) Load structures: gravity-driven sediment mobilization in the shallow subsurface. *Geol Soc* 216(1):21–34
- Owen G, Moretti M, Alfaro P (2011) Recognising triggers for soft-sediment deformation: current understanding and future directions. *Sed Geol* 235(3–4):133–140
- Paxton ST, Szabo JO, Ajdukiewicz JM, Klimentidis RE (2002) Construction of an intergranular volume compaction curve for evaluating and predicting compaction and porosity loss in rigid-grain sandstone reservoirs. *AAPG Bull* 86(12):2047–2067
- Pearce TJ, Martin JH, Cooper D, Wray DS (2010) Chemostratigraphy of upper carboniferous (Pennsylvanian) sequences from the Southern Northsea (United Kingdom). Application of modern stratigraphic techniques: theory and case histories. *SEPM Special Publication No. 94*
- Pearce TJ, Wray D, Ratcliff K, Wright DK, Moscariello A (2005) Chemostratigraphy of the upper carboniferous schooner formation, southern North Sea. In: Collinson JD, Evans DJ, Holliday DW, Jones NS (eds) *carboniferous hydrocarbon geology: The Southern North Sea and surrounding Onshore Areas*. Yorkshire Geological Society, Occasional Publication 7, pp 147–164
- Piessens K, Dusar M (2004) Feasibility of CO<sub>2</sub> sequestration in abandoned coal mines in Belgium. *Geol Belgica* 7(3–4):165–180
- Postma G (1983) Water escape structures in the context of a depositional model of a mass flow dominated conglomeratic fan-delta (Abrijoja Formation, Pliocene, Almeria Basin, SE Spain). *Sedimentology* 30(1):91–103
- Privalov V, Pironon J, de Donato P, Michels R, Morlot C, Izart A (2020) Natural fracture systems in CBM Reservoirs of the Lorraine–Saar coal Basin from the standpoint of X-ray computer tomography. *Environ Sci Proc* 5(1):12
- Quandt D, Busch B, Fuchs H, Alvarado de la Barrera A, Greve J, Hilgers C (2022a) Petrographical and petrophysical properties of tight

- siliciclastic rocks from the Ibbenbueren coal mine with regard to mine flooding. *Zeitschrift Der Deutschen Gesellschaft Für Geowissenschaften* 173(4):653–672
- Quandt D, Busch B, Schmidt C, Hilgers C (2022b) Diagenesis and controls on reservoir quality of Lower Triassic red bed sandstones (Buntsandstein) from a marginal basin facies, southwest Germany. *Mar Pet Geol* 142:105744
- Quandt D, Rudolph T, Hilgers C (2023) Post-mining: geomonitoring, process understanding, and utilization of former mining areas. *Zeitschrift Der Deutschen Gesellschaft Für Geowissenschaften* 173(4):507–511
- Rieckmann M (1970) Untersuchung von Turbulenzerscheinungen beim Fließen von Gasen durch Speichergesteine unter Berücksichtigung der Gleitströmung. *Erdöl-Erdgas-Zeitschrift* 86:36–51
- Rische M, Fischer KD, Friederich W (2023) FloodRisk-Induced seismicity by mine flooding—Observation, characterisation and relation to mine water rise in the eastern Ruhr area (Germany). *Zeitschrift Der Deutschen Gesellschaft Für Geowissenschaften* 173(4):551–564
- Roscher M, Schneider JW (2006) Permo-carboniferous climate: early Pennsylvanian to Late Permian climate development of central Europe in a regional and global context. *Geol Soc* 265(1):95–136
- Rosenau NA, Tabor NJ, Elrick SD, Nelson WJ (2013) Polygenetic history of paleosols in middle–upper Pennsylvanian cyclothems of the Illinois basin, USA: Part I. Characterization of paleosol types and interpretation of pedogenic processes. *J Sediment Res* 83(8):606–636
- Ryan JG, Shervais JW, Li Y, Reagan MK, Li HY, Heaton D, Godard M, Kirchenbauer M, Whattam SA, Pearce JA, Chapman T, Nelson W, Prytulak J, Shimizu K, Petronotis K, IODP Expedition 352 Scientific Team (2017) Application of a handheld X-ray fluorescence spectrometer for real-time, high-density quantitative analysis of drilled igneous rocks and sediments during IODP expedition 352. *Chem Geol* 451:55–66
- Samsonov S, d’Oreye N, Smets B (2013) Ground deformation associated with post-mining activity at the French–German border revealed by novel InSAR time series method. *Int J Appl Earth Obs Geoinf* 23:142–154
- Schäfer A (1986) Die Sedimente des Oberkarbons und Unterrotliegenden im Saar–Nahe-Becken. *Mainzer Geowissenschaftliche Mitteilungen* 15:239–365
- Schäfer A (1989) Variscan molasse in the Saar–Nahe Basin (W-Germany), upper carboniferous and lower Permian. *Geol Rundsch* 78(2):499–524
- Schäfer A (2011) Tectonics and sedimentation in the continental strike-slip Saar–Nahe basin (Carboniferous-Permian, West Germany). *Zeitschrift Der Deutschen Gesellschaft Für Geowissenschaften* 162(2):127–155
- Schäfer A, Korsch RJ (1998) Formation and sediment fill of the Saar–Nahe basin (Permo-Carboniferous, Germany). *Zeitschrift Der Deutschen Geologischen Gesellschaft* 149(2):233–269
- Schäfer A, Sneh A (1983) Lower Rotliegend fluvio-lacustrine sequences in the Saar–Nahe Basin. *Geol Rundsch* 72(3):1135–1145
- Schäfer A, Rast U, Stamm R (1990) Lacustrine paper shales in the Permocarboniferous Saar–Nahe Basin (West Germany)—depositional environment and chemical characterization. In: Heling D, Rothe P, Förstner U, Stoffers P (eds) *Sediments and environmental geochemistry*. Springer, Berlin, pp 220–238
- Scherer M (1987) Parameters influencing porosity in sandstones: a model for sandstone porosity prediction. *AAPG Bull* 71(5):485–491
- Smith TM, Sayers CM, Sondergeld CH (2009) Rock properties in low-porosity/low-permeability sandstones. *Lead Edge* 28(1):48–59
- Stemke M, Wieber G (2022) Closure of German hard coal mines: effects and legal aspects of mine flooding. *Mine Water Environ* 41(1):280–291
- Stollhofen H (1998) Facies architecture variations and seismogenic structures in the Carboniferous-Permian Saar–Nahe Basin (SW Germany): evidence for extension-related transfer fault activity. *Sed Geol* 119(1–2):47–83
- Stollhofen H, Stanistreet IG (1994) Interaction between bimodal volcanism, fluvial sedimentation and basin development in the Permo-Carboniferous Saar–Nahe Basin (south-west Germany). *Basin Res* 6(4):245–267
- Stonecipher SA, Winn Jr, RD, Bishop MG (1984) Diagenesis of the frontier formation, Moxa Arch: a function of sandstone geometry, texture and composition, and fluid flux. In: MacDonald PA, Surdam RC (eds) *clastic diagenesis*. *Am Assoc Petrol Geol Mem vol 37*, pp 289–316
- Svendsen J, Friis H, Stollhofen H, Hartley N (2007) Facies discrimination in a mixed fluvio-eolian setting using elemental whole-rock geochemistry—applications for reservoir characterization. *J Sediment Res* 77(1):23–33
- Taylor TR, Giles MR, Hathon LA, Diggs TN, Braunsdorf NR, Birbiglia GV, Kittridge MG, Macaulay CI, Espejo IS (2010) Sandstone diagenesis and reservoir quality prediction: models, myths, and reality. *AAPG Bull* 94(8):1093–1132
- Tischendorf G, Forster HJ, Gottesmann B, Rieder M (2007) True and brittle micas: composition and solid-solution series. *Mineral Mag* 71(3):285–320
- Trevena AS, Clark RA (1986) Diagenesis of sandstone reservoirs of Pattani Basin, Gulf of Thailand. *AAPG Bull* 70(3):299–308
- Uhl D, Jasper A (2021) Wildfire during deposition of the “Illinger Flözzone” (Heusweiler-Formation, “Stephanian B”, Kasimovian–Ghzelian) in the Saar–Nahe Basin (SW-Germany). *Palaeobiodivers Palaeoenvir* 101(1):9–18
- Virgo S, Abe S, Urai JL (2014) The evolution of crack seal vein and fracture networks in an evolving stress field: insights from discrete element models of fracture sealing. *J Geophys Res Solid Earth* 119(12):8708–8727
- Walderhaug O (1994) Temperatures of quartz cementation in Jurassic sandstones from the Norwegian continental shelf; evidence from fluid inclusions. *J Sediment Res* 64(2a):311–323
- Walton AW, Wojcik KM, Goldstein RH, Barker CE (1995) Diagenesis of upper carboniferous rocks in the Ouachita foreland shelf in mid-continent USA: an overview of widespread effects of a Variscan-equivalent orogeny. *Geol Rundsch* 84:535–551
- Wiltshko DV, Morse JW (2001) Crystallization pressure versus “crack seal” as the mechanism for banded veins. *Geology* 29(1):79–82
- Wirth P, Mali BČ, Fischer W (2012) Problems and potentials of post-mining regions. Post-mining regions in Central Europe—problems, potentials, possibilities. *oekom verlag, Gesellschaft für ökologische Kommunikation mbH, München*
- Worden RH, Armitage PJ, Butcher AR, Churchill JM, Csoma AE, Hollis C, Lander RH, Omma JE (2018) Petroleum reservoir quality prediction: overview and contrasting approaches from sandstone and carbonate communities. *Geol Soc Lond Special Publ* 435(1):1–31
- Worden RH, Griffiths J, Wooldridge LJ, Utley JEP, Lawan AY, Muhammed DD, Simon N, Armitage PJ (2020) Chlorite in sandstones. *Earth Sci Rev* 204:103105
- Wüstefeld P, Hilse U, Koehrer B, Adelman D, Hilgers C (2017a) Critical evaluation of an upper carboniferous tight gas sandstone reservoir analog: diagenesis and petrophysical aspects. *Mar Pet Geol* 86:689–710
- Wüstefeld P, Hilse U, Lüders V, Wemmer K, Koehrer B, Hilgers C (2017b) Kilometer-scale fault-related thermal anomalies in tight gas sandstones. *Mar Pet Geol* 86:288–303
- Young KE, Evans CA, Hodges KV, Bleacher JE, Graff TG (2016) A review of the handheld X-ray fluorescence spectrometer as a tool for field geologic investigations on Earth and in planetary surface exploration. *Appl Geochem* 72:77–87